8398 *Biochemistry* **2010,** *49,* 8398–8414
DOI: 10.1021/bi100698n

BIOCHEMISTRY
including biophysical chemistry & molecular biology
Article

Characterization of the *N*-Acetyl-α-D-glucosaminyl L-Malate Synthase and Deacetylase Functions for Bacillithiol Biosynthesis in *Bacillus anthracis*[†,‡]

Derek Parsonage,[§,○] Gerald L. Newton,[∇,○] Robert C. Holder,[‖] Bret D. Wallace,[⊥] Carleitta Paige,[§,●] Chris J. Hamilton,[#] Patricia C. Dos Santos,[@] Matthew R. Redinbo,[⊥] Sean D. Reid,[‖] and Al Claiborne*[,§]

[§]*Center for Structural Biology, and* [‖]*Department of Microbiology and Immunology, Wake Forest University School of Medicine, Winston-Salem, North Carolina 27157,* [⊥]*Department of Chemistry and Department of Biochemistry and Biophysics, University of North Carolina, Chapel Hill, North Carolina 27599-3290,* [@]*Department of Chemistry, Wake Forest University, Winston-Salem, North Carolina 27109,* [#]*School of Chemical Sciences and Pharmacy, University of East Anglia, Norwich NR4 7TJ, England, and* [∇]*Department of Chemistry and Biochemistry, University of California, San Diego, La Jolla, California 92093-0314.*
[○]*These authors contributed equally to this work.* [●]*Present address: Department of Natural Sciences, Virginia Union University, Richmond, VA 23220.*

Received May 5, 2010; Revised Manuscript Received August 25, 2010

ABSTRACT: Bacillithiol (Cys-GlcN-malate, BSH) has recently been identified as a novel low-molecular weight thiol in *Bacillus anthracis*, *Staphylococcus aureus*, and several other Gram-positive bacteria lacking glutathione and mycothiol. We have now characterized the first two enzymes for the BSH biosynthetic pathway in *B. anthracis*, which combine to produce α-D-glucosaminyl L-malate (GlcN-malate) from UDP-GlcNAc and L-malate. The structure of the GlcNAc-malate intermediate has been determined, as have the kinetic parameters for the *Ba*BshA glycosyltransferase (→GlcNAc-malate) and the *Ba*BshB deacetylase (→GlcN-malate). BSH is one of only two natural products reported to contain a malyl glycoside, and the crystal structure of the *Ba*BshA–UDP–malate ternary complex, determined in this work at 3.3 Å resolution, identifies several active-site interactions important for the specific recognition of L-malate, but not other α-hydroxy acids, as the acceptor substrate. In sharp contrast to the structures reported for the GlcNAc–1-D-*myo*-inositol-3-phosphate synthase (MshA) apo and ternary complex forms, there is no major conformational change observed in the structures of the corresponding *Ba*BshA forms. A mutant strain of *B. anthracis* deficient in the BshA glycosyltransferase fails to produce BSH, as predicted. This *B. anthracis bshA* locus (BA1558) has been identified in a transposon-site hybridization study as required for growth, sporulation, or germination [Day, W. A., Jr., Rasmussen, S. L., Carpenter, B. M., Peterson, S. N., and Friedlander, A. M. (2007) *J. Bacteriol. 189*, 3296–3301], suggesting that the biosynthesis of BSH could represent a target for the development of novel antimicrobials with broad-spectrum activity against Gram-positive pathogens like *B. anthracis*. The metabolites that function in thiol redox buffering and homeostasis in *Bacillus* are not well understood, and we present a composite picture based on this and other recent work.

In his recent review of the management of oxidative stress in *Bacillus*, Zuber (*1*) concludes that the metabolites that function in redox buffering and thiol homeostasis, and their influence on the oxidative stress response, are not well understood. Earlier work from this laboratory (*2*) demonstrated that CoASH provided the major low-molecular weight thiol redox buffer in *Bacillus anthracis*, replacing GSH as had previously been demonstrated for *Staphylococcus aureus* (*3*). The likelihood that CoASH plays an important functional role in redox buffering and thiol homeostasis is strengthened by the demonstration that both *B. anthracis* (*4*) and *S. aureus* (*3*, *5*–*7*) have NAD(P)H-dependent coenzyme A-disulfide reductases (CoADRs).[1] We have also shown that the type III pantothenate kinase, which is unusual in its insensitivity to feedback inhibition by CoASH (*2*), is essential for growth of *B. anthracis* (*8*). CoADR, the chimeric CoADR-RHD protein (*9*), and the type III pantothenate kinase represent three well-characterized adaptations of the CoASH-based redox buffer system for this Gram-positive pathogen.

A new unknown thiol, originally termed U12, was also identified in the *B. anthracis* extract (*2*); a mass of 398 Da was reported for U12-SH. Via the combination of analytical chemical approaches with mass spectrometry and NMR, the structure of U12 has been determined to be *N*-cysteinyl-α-D-glucosaminyl L-malate,

---

[†] This work was supported by National Institutes of Health Grants GM-35394 (A.C.), AI-78924 (M.R.R.), and AI-72133 (G.L.N.; Robert C. Fahey, Principal Investigator).

[‡] Coordinates have been deposited in the Protein Data Bank as entry 3MBO.

*To whom correspondence should be addressed. Telephone: (336) 716-3914. Fax: (336) 777-3242. E-mail: alc@csb.wfu.edu.

[1] Abbreviations: CoADR, coenzyme A-disulfide reductase; CoADR-RHD, coenzyme A-disulfide reductase isoform with a C-terminal rhodanese homology domain; BSH, bacillithiol; BshA, *N*-acetyl-α-D-glucosaminyl L-malate synthase; GlcNAc-malate, *N*-acetyl-α-D-glucosaminyl L-malate; BshB, *N*-acetyl-α-D-glucosaminyl L-malate deacetylase; GlcN-malate, α-D-glucosaminyl L-malate; MshA, *N*-acetyl-α-D-glucosaminyl 1-D-*myo*-inositol-3-phosphate synthase; Ins, *myo*-inositol; MSH, mycothiol; GT, glycosyltransferase; *Bc*ZBP, *Bacillus cereus* zinc-binding protein; MshB, *N*-acetyl-α-D-glucosaminyl 1-D-*myo*-inositol-3-phosphate deacetylase; BHI, Brain Heart Infusion; LB, Luria-Bertani; Ery^{R}, erythromycin-resistant; Tet^{R}, tetracycline-resistant; HEPES, *N*-(2-hydroxyethyl)-piperazine-*N*′-2-ethanesulfonic acid; HPLC, high-performance liquid chromatography; ESP, electrospray; gCOSY, gradient correlation spectroscopy; RSmB, methylbimane derivative of thiol, RSH, from reaction with monobromobimane; Mca, mycothiol *S*-conjugate amidase; TrxR, thioredoxin reductase; Trx, thioredoxin; Grx, glutaredoxin.

and U12 has been renamed bacillithiol [BSH (*10*)]. BSH is present at intracellular concentrations of 0.1−0.35 mM[2] in a number of *Bacillus* species, including *B. anthracis*, *Bacillus subtilis*, and *Bacillus megaterium*, as well as in *S. aureus*. While none of the four *B. subtilis* strains represented in the NCBI database have orthologs of CoADR or any of its isoforms (*9*), *B. anthracis*, *B. megaterium* (*11*), and *S. aureus* (*3*) maintain both CoASH and BSH redox buffer systems, in the absence of GSH. Pöther et al. (*12*), in a recent study with *S. aureus* demonstrating that the majority of reversible protein thiol oxidations observed during treatment of cells with diamide are based on *S*-thiolations with Cys rather than protein disulfide formation, have concluded that Cys also functions as an important thiol redox buffer in *S. aureus*.

In an initial study of the biosynthesis and functions of BSH (*13*), we have demonstrated that the *B. subtilis* YpjH protein (*Bsu*BshA), the enzyme orthologous to *B. anthracis* ORF BA1558, catalyzes the synthesis of *N*-acetyl-α-D-glucosaminyl L-malate (GlcNAc-malate) from UDP-GlcNAc and L-malate; the product structure has been confirmed by mass spectrometry (*10*, *13*). We have also demonstrated that the BA1557 gene product (*Ba*BshB) catalyzes the deacetylation of GlcNAc-malate (*13*), providing the free 2-amino group of the GlcN moiety required for the Cys ligation step that is proposed to complete the synthesis. Deletion of the *B. subtilis yllA* locus, predicted to be involved in the biosynthetic pathway and initially suggested to encode this putative ligase, does eliminate BSH production; the recombinant protein, however, does not catalyze ATP-dependent BSH formation from Cys and GlcN-malate, as assayed in vitro.

In the absence of functional information, Ruane et al. (*14*) have reported the structure of the ORF BA1558 (identified in this work as *Ba*BshA) apoenzyme, refined at a resolution of 3.1 Å. Although this enzyme, like the MshA glycosyltransferase that produces GlcNAc-Ins-P in the first step of mycothiol (MSH) biosynthesis (*15*, *16*), is a member of the GT-B and GT4 fold (*17*) and Carbohydrate-Active enZymes (*18*) families, structural homology searches using the MshA apoenzyme structure were unsuccessful in identifying other GT-B family members, including ORF BA1558. This indicates a major conformational difference between the two apoenzymes, despite the similarity in the reactions catalyzed. Fadouloglou et al. (*19*) reported the crystal structure of the Zn^{2+}-binding *Bc*ZBP protein from *Bacillus cereus*, as refined at a resolution of 1.8 Å. *Bc*ZBP is the enzyme orthologous to *Ba*BshB, the GlcNAc-malate deacetylase, with 97% sequence identity. A recent kinetic analysis (*20*) with GlcNAc and several GlcNAc oligomers indicated that, although the biological function and natural substrate for *Bc*ZBP were unknown, the enzyme had optimal activity with $(GlcNAc)_2$ ($k_{cat}/K_m = 3.3 \times 10^7\ M^{-1}\ s^{-1}$ at 37 °C). The enzyme is a member of the PIG-L superfamily represented by GlcNAc-phosphatidylinositol deacetylase (*21*), the MshB deacetylase (*22*) of the MSH biosynthetic pathway, and the mycothiol *S*-conjugate amidase (*23*). The active-site Zn^{2+} of *Bc*ZBP is buried at the bottom of a ca. 12 Å deep cavity on the hexamer surface, and Arg140 is prominently positioned at the entry of the cavity. Both R140A and R140E mutants exhibit k_{cat}/K_m values that are 0.2−0.3% of that of the wild-type enzyme (*20*). His12, Asp15, and His113 provide the protein ligands to the Zn^{2+}, and Asp14 has been proposed as an acid−base catalyst in the hydrolase reaction. A model of a *Bc*ZBP−GlcNAc complex reveals that this substrate is considerably smaller than the volume of the cavity; a hydrophilic patch consisting of the side chains of Asp108, Asn150, and Tyr194 marks an unoccupied region proximal to the Zn^{2+}. The Y194F mutant specificity constant, which is $< 0.1\%$ of that of the wild type (*20*), reflects a dominant effect on K_m. In particular, the anomeric C1-OH group of GlcNAc also appears to be accommodated by a relatively large space within the cavity. For the *Bc*ZBP apoenzyme structure, three very mobile loops have recently been implicated in determining active-site accessibility and regulating substrate specificity (*24*).

Given the goal of improving the definition of the thiol redox buffer in *B. anthracis* and characterizing potential new targets for the development of antimicrobial agents that are selective against *B. anthracis*, *S. aureus*, and other Gram-positive pathogens that rely on the BSH-based redox buffer system, we report here detailed kinetic analyses of the *Ba*BshA glycosyltransferase and *Ba*BshB deacetylase. The kinetic studies are interpreted in view of the ORF BA1558 and *Bc*ZBP crystal structures, and we also provide the structure of the *Ba*BshA−UDP−malate complex, refined at a resolution of 3.3 Å, which demonstrates the absence of any major conformational change on ligand binding. In addition, we show that deletion of the BAS1445 locus encoding BshA in *B. anthracis* Sterne generates a BSH-deficient strain appropriate for testing in a murine model of inhalational anthrax.

EXPERIMENTAL PROCEDURES

Bacterial Strains and Antibiotics. The *B. anthracis* Sterne 34F2 strain ($pXO1^+$ $pXO2^-$) used in these studies was obtained from P. Hanna (University of Michigan Medical School, Ann Arbor, MI). Cultures were grown and maintained in BHI broth (Difco) and on solid media containing 15 g of agar per liter. For preparation of parental and mutant endospores, cultures were grown at 37 °C on BHI plates containing antibiotics as appropriate. A single colony was inoculated into 3 mL of BHI broth containing antibiotics as required, and this culture was taken as the inoculum (5%, v/v) into 75 mL of fresh modified G (sporulation) medium (*25*) without antibiotic, after having grown for 8−12 h. After having grown for 4 days at the appropriate temperature, endospores were collected by centrifugation, and residual vegetative cells were killed by a 30 min incubation at 65 °C. Pellets were washed three or four times in deionized water, and endospores were stored (in deionized water) at ambient temperature. The purity of the spore preparations was confirmed by phase-contrast microscopy, and spore titers were determined by serial dilution. *Escherichia coli* strains DB3.1 (*26*) and GM272 were used for the cloning and propagation of pBKJ236 and pBKJ223 (*27*), respectively. DB3.1(pBKJ236) was cultured and maintained in LB broth or on solid media supplemented with 250−400 μg/mL erythromycin. GM272(pBKJ223) was cultured and maintained in LB broth or on solid media supplemented with 15 μg/mL tetracycline.

Construction of B. anthracis Sterne Deletion Strains. In-frame deletion mutants of the genes encoding *Ba*BshA (*bshA*, loci BA1558 and BAS1445 in Ames and Sterne strains, respectively), *Ba*BshB (*bshB*, loci BA1557 and BAS1444, respectively), *Ba*CoADR [*cdr*, loci BA1263 (*4*) and BAS1170, respectively], and *Ba*CoADR-RHD [*cdr2*, loci BA0774 (*9*) and BAS0736, respectively] were constructed following the markerless gene replacement protocol (*27*), using the pBKJ236 and pBKJ223

---

[2] Intracellular concentrations are calculated from BSH contents (micromoles per gram of dry weight), using a value of 2 μL/mg of dry weight for the cell volume (*2*).

plasmids. The procedure followed in this work is described in detail for the BASΔ1445 mutant. A modified chromosomal segment containing the BAS1445 deletion was constructed by first amplifying the flanking upstream and downstream regions (>500 bp each) using primer sets BAS1445up (FWD/REV) and BAS1445dwn (FWD/REV), respectively (Table S1 of the Supporting Information). The two amplified products were then ligated using overlap polymerase chain reaction (PCR) with BAS1445up FWD/BAS1445dwn REV, and the resulting deletion fragment was TA cloned into pCR2.1 (Invitrogen) before being subcloned into pBKJ236 digested with *Not*I. This plasmid, pBKJ236::BAS1445′, was electroporated into methylation-deficient (*dam*$^-$ *dcm*$^-$) *E. coli* GM272. *E. coli* GM272-(pBKJ236::BAS1445′) (LB broth with 250 μg/mL erythromycin), *E. coli* helper strain 459 (LB broth with 100 μg/mL ampicillin), and *B. anthracis* Sterne were grown overnight, and aliquots (75 μL) from washed samples of each culture were mixed and spotted onto BHI agar before being incubated for 48 h at room temperature. The accumulated growth was resuspended in fresh LB broth, and 150 μL of the suspension was dispensed in a "straight line" on one quadrant of a BHI agar plate supplemented with 5 μg/mL erythromycin and 80 units/mL polymyxin B. After the line was allowed to dry, cells were streaked to isolation and incubated at room temperature for 48 h. Isolated Ery^R colonies were cultured overnight, again at room temperature, before being diluted 1:1000 in fresh BHI broth with erythromycin and shifted to 37 °C, a nonpermissive temperature for plasmid replication. Following this overnight incubation, integrants were isolated using the straight line procedure described above, but with incubation at 37 °C on BHI agar with erythromycin. A single Ery^R colony was grown out, to an A_{600} of ~0.2, in 25 mL of LB broth with glucose (*28*) at 37 °C, with shaking at 100 rpm; cells were harvested by centrifugation at 4 °C, resuspended and washed in ice-cold electrotransformation buffer (*29*), and transferred (400 μL) to a chilled 0.4 cm electrode-gap cuvette. After incubation on ice for 10 min, with 5 μL of unmethylated pBKJ223 [isolated from *E. coli* GM272(pBKJ223)], cells were electroporated at 2.4 kV, 200 Ω, and 25 μF. After being pulsed, cells were placed back on ice, and 700 μL of ice-cold LB broth with glucose was added; the mixture was transferred to a microcentrifuge tube, and cells were allowed to recover for 3 h at 30 °C before being plated on BHI agar with 10 μg/mL tetracycline and incubated overnight at 37 °C. Several single Tet^R colonies selected after being repeatedly mixed and streaked to isolation were patched onto BHI agar with erythromycin and BHI agar with tetracycline and incubated overnight at 37 °C. Clones with the desired Tet^R Ery^S (loss of pBKJ236) phenotype were validated by colony PCR, repurified by streaking, and patched onto BHI agar with and without tetracycline. Clones cured of Tet^R (loss of pBKJ223) were again validated by colony PCR to confirm the BAS1445 deletion. Δ*bshB*, Δ*cdr*, and Δ*cdr2* mutants were constructed following the same protocol; the Δ*cdr*Δ*cdr2* double mutant utilized the Δ*cdr* strain in the initial conjugation step.

Fosfomycin Sensitivity of Wild-Type and Δ*bsh Strains.* An active culture grown to an A_{600} of 0.5 (midlog) was used to inoculate (1%, v/v) 5 mL aliquots of fresh BHI broth containing fosfomycin at incremental concentrations. The wild-type Sterne strain showed robust growth (static conditions in 17 mm × 100 mm polystyrene tubes) at all fosfomycin concentrations (0−1000 μg/mL). The Δ*bshA* mutant grew only in the control (no fosfomycin) culture and at the lowest fosfomycin concentration tested (200 μg/mL), but not at concentrations of ≥400 μg/mL. The Δ*bshB* mutant was sensitive to fosfomycin at 800 μg/mL, but not at ≤400 μg/mL.

Expression and Purification of B. anthracis BshA, BshB, and CysS. The codon-optimized BA1558 and BA1557 genes, encoding *Ba*BshA and *Ba*BshB, respectively, were synthesized by GenScript (Piscataway, NJ) and subcloned into pET28a(+) (Novagen). Both genes were expressed in *E. coli* BL21(DE3) cells using autoinduction medium at 37 °C (*30*); BshA was expressed with an N-terminal His tag (see Results), while BshB had a C-terminal His tag (-LEH$_6$). All steps of both purifications were conducted at 4 °C. Harvested cells were disrupted using an Avestin EmulsiFlex-C5 homogenizer, and nucleic acids were removed by addition of 2% streptomycin sulfate and centrifugation (27000*g* for 20 min). For BshA, the clarified extract was loaded onto a 25 mL Ni Sepharose High Performance column (GE Healthcare, Piscataway, NJ) in 50 mM sodium phosphate (pH 8.0) containing 0.3 M NaCl and 20 mM imidazole; the protein was eluted with a stepwise increase in the imidazole concentration, to 250 mM. Peak fractions were pooled and loaded onto a Q-Sepharose HP column after dialysis against 20 mM HEPES (pH 7.5) containing 50 mM NaCl. The protein was eluted with a linear 375 mL gradient from 0.05 to 1 M NaCl, and the *Ba*BshA pool was dialyzed against the Q-Sepharose loading buffer before being concentrated and stored in aliquots at −80 °C. For *Ba*BshB, the immobilized metal ion affinity chromatography column was first converted to the Zn^{2+} form (*31*); the clarified extract was loaded onto the 25 mL Zn Sepharose column in 50 mM sodium phosphate (pH 8.0) containing 0.3 M NaCl and 20 mM imidazole. The protein was eluted with a stepwise increase in the imidazole concentration, to 250 mM. Peak fractions were pooled and loaded onto a Q-Sepharose HP column after dialysis against 25 mM potassium phosphate (pH 7.0). The protein was eluted with a linear 375 mL gradient from 0 to 1 M NaCl, and the purified *Ba*BshB protein was dialyzed against 25 mM Tris-HCl (pH 8.0) containing 50 mM NaCl, concentrated by ultrafiltration, and brought to a final concentration of 20% (v/v) glycerol before being frozen in aliquots at −80 °C.

The cysteinyl-tRNA synthetase gene (*cysS*, BA0089) was amplified from genomic *B. anthracis* DNA using primers designed with *Nco*I and *Xho*I linkers that allowed cloning into pET28a. The recombinant C-terminal His-tagged CysS protein was expressed in *E. coli* BL21(DE3); cultures grown to midlog phase in LB broth with kanamycin at 37 °C were induced with lactose for 3 h. Harvested cells were resuspended in 1.5 volumes of degassed 50 mM Tris-HCl (pH 8.0) containing 0.5 M NaCl and were lysed with a French press. The extract was clarified by centrifugation and applied to a Ni^{2+}-charged metal-ion affinity column (GE Healthcare) equilibrated with lysis buffer; the column was washed with this buffer containing 20 mM imidazole before the recombinant CysS protein was eluted with 100 mM imidazole. Pooled fractions were diluted with 5 volumes of lysis buffer and loaded onto a HiTrap Q XL column (GE Healthcare); the column was washed with lysis buffer before the protein was eluted with a linear 50 mL gradient from 0 to 1 M NaCl. The cysteine adenylation activity of *B. anthracis* CysS was assayed using the ATP−^{32}PP$_i$ exchange reaction in the presence of 50 μM Cys (*32*).

Enzymatic Synthesis of GlcNAc-malate. GlcNAc-malate required for kinetic analysis of *Ba*BshB was produced on a preparative scale via incubation of 0.5 mg of *Ba*BshA at 37 °C with 50 μmol each of UDP-GlcNAc and L-malate (substrates purchased from Sigma) in 5 mL of 25 mM HEPES (pH 7.5) containing 100 mM NaCl, 10 mM $MgCl_2$, and 1 mM 2-mercaptoethanol. The reaction mixture was sampled at the indicated times; samples were processed as described by Newton et al. (*15*) for identification of the MshA-catalyzed reaction products (using unlabeled substrates) and were analyzed by HPLC with A_{260} detection for UDP-GlcNAc and UDP. The conversion of UDP-GlcNAc to UDP was complete in 2 h. The GlcNAc-malate product (50 μmol, ca. 15 mg) was processed for preparative HPLC purification by (1) addition of 1 volume of acetonitrile to the reaction mixture and incubation at 60 °C for 15 min, (2) clarification by centrifugation, and (3) adjustment of the supernatant to pH 3 with trifluoroacetic acid after the volume had been reduced to 2 mL in a SpeedVac. A Vydac 218TP1022 (1 cm × 25 cm) reversed-phase preparative column was used with a linear gradient from 0 to 20% methanol in 0.1% trifluoroacetic acid, over 40 min (flow rate of 5 mL/min), with online detection by mass spectrometry. Fractions containing GlcNAc-malate (ESP^-, *m*/*z* 336) were combined, and the separation was repeated to obtain the purified product, which was adjusted to pH 6 with NaOH and lyophilized.

Synthetic GlcNAc-malate was maintained at −70 °C in H_2O at a concentration of 80 mM and contained ca. 1 equiv of sodium trifluoroacetate from the HPLC solvent. The sodium trifluoroacetate content was determined in the quantitative pH titration described above. In addition, the disodium GlcNAc-malate content determined by the *Ba*BshB−Accu-Tag method (see below) accounts for ca. 50% of the total mass of the lyophilized material. ^1H and gCOSY NMR spectra were recorded on a Jeol ECA500 instrument at 500 MHz and were referenced to residual solvent (HDO) at 4.8 ppm. The ^1H NMR of GlcNAc-malate in D_2O (trifluoroacetate is not observable) confirmed the absence of other organic impurities. ^{13}C spectra were recorded on a Varian X500 instrument (125 MHz) equipped with an XSens cold probe. All spectra were recorded at 23 °C. High-resolution mass spectrometry analysis was provided by the UCSD Chemistry and Biochemistry Mass Spectrometry Facility using a Thermo Scientific LTQ Orbitrap XL mass spectrometer operating in positive ion mode ESP ionization.

BaBshA and BaBshB Kinetic Parameters. The kinetic properties of *Ba*BshA were first analyzed from initial rates of UDP-GlcNAc to UDP conversion, using the A_{260}-based HPLC assay described above (*15*) for monitoring GlcNAc-malate synthesis. Initial rates were determined over a range of UDP-GlcNAc concentrations (0−25 mM) at a fixed concentration of 2 mM L-malate (ca. $15K_m$; see Results); for each individual assay at 37 °C [in 25 mM HEPES (pH 7.5) containing 100 mM NaCl, 10 mM $MgCl_2$, and 1 mM 2-mercaptoethanol], the reaction mixture was sampled four times to establish the observed rate of UDP formation. Similarly, initial rates were measured over a series of L-malate concentrations (0−3.2 mM) at a fixed concentration of 3 mM UDP-GlcNAc (ca. $5K_m$). Results representing the mean of triplicate determinations were fit to the Michaelis−Menten equation [eq 1 (*33*)]

$$v = (V_{\max}A)/(K_A + A) \tag{1}$$

where $V_{\max}$ is the apparent maximal velocity, A is the concentration of the varied substrate, and K_A is the Michaelis constant (apparent) for substrate A. Data described with this single-variable equation were analyzed using KaleidaGraph.

To analyze the steady-state kinetic mechanism with several fixed concentrations of UDP-GlcNAc and L-malate, the continuous spectrophotometric assay for glycosyltransferases (*34*) was adapted, using a 96-well format with a POLARstar OPTIMA (BMG LABTECH) microplate reader. For each assay at 37 °C, 30 ng of *Ba*BshA was incubated in 25 mM HEPES (pH 7.5) containing 50 mM KCl, 10 mM $MgCl_2$, 7.5 units of pyruvate kinase and 15 units of lactate dehydrogenase (both enzymes purchased from Sigma), 0.8 mM phosphoenolpyruvate, and 0.15 mM NADH in a final volume of 200 μL. The concentration of L-malate was varied over the range of 0.08−1.2 mM at fixed UDP-GlcNAc concentrations of 0.1−1.5 mM. Reactions were initiated by addition of enzyme and were performed in duplicate. These results (for varying L-malate concentrations) were fit to the reciprocal form of the velocity equation for a rapid equilibrium random system [eq 2 (*33*)], using GraFit version 5.

$$\frac{1}{v} = \frac{\alpha K_{\mathrm{Acc}}}{V_{\max}}\left(1 + \frac{K_{\mathrm{Don}}}{[\mathrm{Don}]}\right)\left(\frac{1}{[\mathrm{Acc}]}\right) + \frac{1}{V_{\max}}\left(1 + \frac{\alpha K_{\mathrm{Don}}}{[\mathrm{Don}]}\right) \tag{2}$$

where Don is UDP-GlcNAc and Acc is L-malate. α is a factor representing the effect each substrate has on the binding of the second substrate. Controls showed that the omission of 2-mercaptoethanol and substitution of 50 mM KCl for 100 mM NaCl in the coupled assay had no effect on the initial velocity. In addition, any competitive UDP-GlcNAc hydrolysis reaction (measured in the absence of L-malate) was negligible.

The kinetic parameters for *Ba*BshB were determined from initial rates of GlcNAc-malate → GlcN-malate conversion, using an HPLC assay for the AccQ-Tag derivative of the GlcN-malate product, as monitored by fluorescence (*13*, *31*, *35*). Initial rates were determined over a series of GlcNAc-malate concentrations (0−2 mM); for each assay at 37 °C [in 50 mM HEPES (pH 7.5) containing 50 mM NaCl and 1 equiv of sodium trifluoroacetate per mole of GlcNAc-malate], the reaction mixture was sampled at intervals to establish the rate of GlcN-malate formation. Results representing the mean of triplicate determinations were fit to eq 1 as described above. Bacillithiol *S*-conjugate amidase activity was measured using the methylbimane derivative of BSH (BSmB) purified as described previously (*10*). The reaction mixture was sampled at intervals; aliquots were processed for analysis, using an adaptation of the fluorescence-based HPLC assay for CySmB (plus GlcN-malate) product formation described previously (*23*). The initial rate of CySmB formation was determined by sampling the reaction mixture four times in the presence of 320 μM BSmB.

Crystallographic Methods. After purification, *Ba*BshA was buffer-exchanged into 20 mM HEPES (pH 7.5) containing 150 mM NaCl and 5 mM dithiothreitol and concentrated to 16 mg/mL for crystallization. Crystals were obtained in 0.2 M $Mg(HCO_2^-)_2$ containing 15% PEG3350 with 1 mM UDP and 1 mM L-malate. Crystals were cryoprotected with mother liquor supplemented with 25% glycerol and flash-frozen in liquid nitrogen. *Ba*BshA crystals, which appeared after 4−5 days, diffracted to 3.3 Å. Data sets were collected at SER-CAT beamline 22-BM (Advanced Photon Source, Argonne National Laboratory, Argonne, IL). Data were indexed and scaled using HKL2000 (*36*). Molecular replacement was performed using PHASER (*37*), and model refinement was conducted using the PHENIX software suite (*38*). The model was adjusted manually using COOT (*39*) as well as $2F_o - F_c$ and $F_o - F_c$ electron density maps. The UDP and L-malate model and definition files were generated with PHENIX.

Analysis of Thiols from Wild-Type and Mutant Strains of B. anthracis. All manipulations of *B. anthracis* Sterne strains were conducted under Biosafety Level 2 conditions at Wake Forest University School of Medicine and at the University of California, San Diego. The detailed methods for culture growth, sample preparation, and analysis, including the determination of thiol redox status, are described by Nicely et al. (*2*) and Newton et al. (*10*).

Bioinformatics. Sequence analyses were performed with the NCBI and PDB databases using BLASTP, and the resources of the Carbohydrate-Active enZymes database (*18*) were also utilized in this work. Structure superpositions and sequence alignments were performed using DALILITE (*40*), PyMOL (*41*), CLUSTALW (*42*), and ESPript (*43*). Figures of protein molecules and residues were prepared using PyMOL.

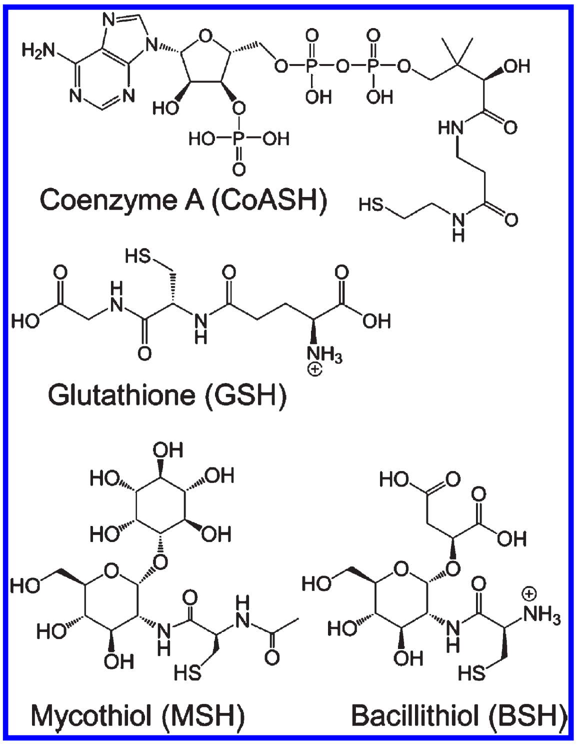

FIGURE 1: Low-molecular weight thiol redox buffers.

RESULTS

Proposed BSH Biosynthetic Pathway in B. anthracis. Given the structural similarity between bacillithiol and mycothiol (Figure 1) and the well-defined pathway for MSH biosynthesis in *Mycobacterium tuberculosis* and other *Actinobacteria* (*44*, *45*), three distinct enzymatic steps have been considered in the pathway for BSH biosynthesis (Figure 2). The first reaction produces GlcNAc-malate from UDP-GlcNAc and L-malate, as indicated:

$$\text{UDP-GlcNAc} + \text{L-malate} \rightarrow \text{GlcNAc-malate} + \text{UDP} \qquad (\text{I})$$

We have demonstrated (*13*) that the *B. subtilis* YpjH gene product catalyzes the synthesis of GlcNAc-malate as given in reaction I. In *B. anthracis*, the BA1558 locus is the ortholog of *B. subtilis ypjH*; as shown in the preparative scale assay (Figure S1 of the Supporting Information), ORF BA1558 catalyzes the production of UDP and GlcNAc-malate when incubated with UDP-GlcNAc and L-malate. Isolation of the GlcNAc-malate product from this preparative scale reaction mixture allowed its confirmation by ^{1}H and ^{13}C NMR (Figure S2 of the Supporting Information) and high-resolution mass spectrometry. The proton NMR spectra (Figure S2A of the Supporting Information) indicated that the GlcNAc-malate was pure (see Experimental Procedures) and contained the L-malate and D-glucosamine resonances found in bacillithiol (*10*). The glucosamine *N*-acetyl group is validated by the acetyl protons (singlet, 2.04 ppm) and the carbon resonances at 174.3 and 21.9 ppm (Figure S2B of the Supporting Information). The C2 proton (3.9 ppm) of glucosamine (nitrogen-bound carbon) is identified in the gCOSY spectra (Figure S2A of the Supporting Information) by correlation with the anomeric proton. The anomeric proton (4.89 ppm) coupling constant (3.8 Hz) indicated this was the α-anomer of the malyl glycoside as predicted by the structure of bacillithiol. The high-resolution mass spectra of this compound gave a mass of 360.0902 for the sodium ion of GlcNAc-malate (360.0901, δ 0.3 ppm) corresponding to a formula of $C_{12}H_{19}NO_{10}Na$, consistent with the product of *Ba*BshA. Confirmation of the novel D-glucosaminyl L-(α)-malate moiety validates the structure of bacillithiol from *Deinococcus radiodurans* (*10*) and shows that it is identical to that of bacillithiol produced in *B. anthracis*. ORF BA1558 is the BshA glycosyltransferase in *B. anthracis* and is therefore designated *Ba*BshA (Figure 2).

When the structure of the *M. tuberculosis* GlcNAc-Ins deacetylase MshB [Protein Data Bank (PDB) entry 1Q74 (*22*)] was

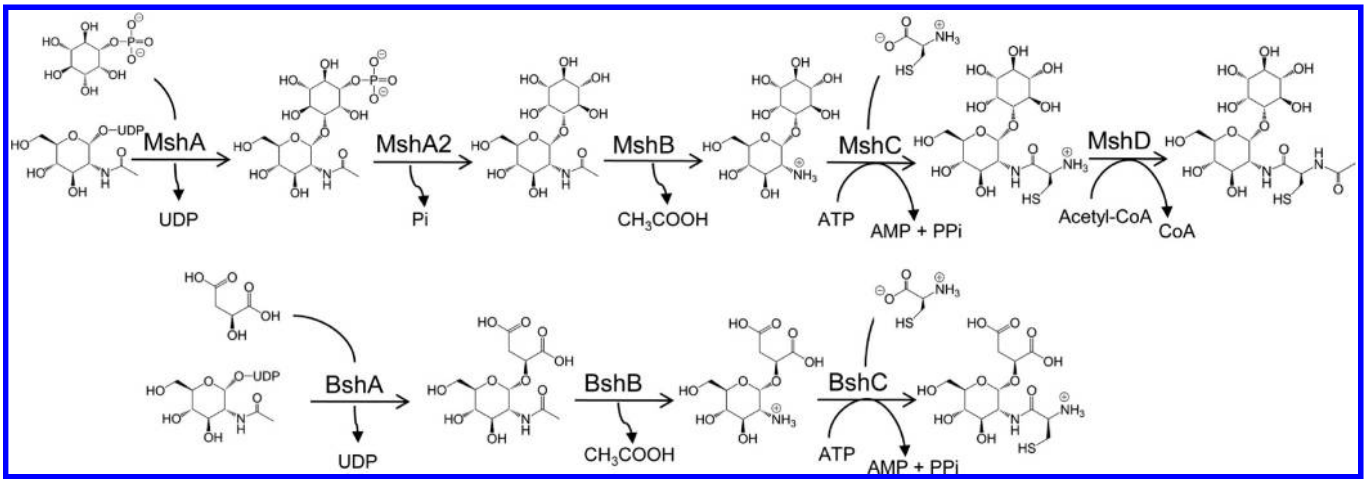

FIGURE 2: Mycothiol biosynthetic pathway (top) and proposed bacillithiol biosynthetic pathway (bottom).

Table 1: Bioinformatics of the *B. anthracis bsh* and *pan* Operons

gene	functional homologue/PDB entry[a]	comparison
BA1554	putative pyrophosphatase YpjD/2GTA (*B. subtilis*)	74% identical, *E* value of 4×10^{-45}
BA1555 (*dapB*)	dihydrodipicolinate reductase/1YL6 (*M. tuberculosis*)	44% identical, *E* value of 3×10^{-48}
BA1556 (*mgsA*)	methylglyoxal synthase/1B93 (*E. coli*)	50% identical, *E* value of 2×10^{-32}
BA1557 (*bshB*)	GlcNAc-malate deacetylase/2IXD (*B. cereus*)	96% identical, *E* value of 6×10^{-133}
BA1558 (*bshA*)	GlcNAc-malate synthase/2JJM	identical
BA1559 (*pcnB*)	tRNA CCA-adding enzyme/1MIY (*Bacillus stearothermophilus*)	49% identical, *E* value of 4×10^{-106}
BA1560 (*birA*)	biotin:CoASA*c* carboxylase ligase/1WNL (*Pyrococcus horikoshii*)	32% identical, *E* value of 7×10^{-36}
BA1562 (*panB*)	ketopantoate hydroxymethyltransferase/1M3U (*E. coli*)	46% identical, *E* value of 1×10^{-63}
BA1563 (*panC*)	pantothenate synthetase/2X3F (*S. aureus*)	53% identical, *E* value of 2×10^{-87}
BA1564 (*panD*)	aspartate decarboxylase proenzyme/2C45 (*M. tuberculosis*)	55% identical, *E* value of 1×10^{-33}
BA1565	putative PolC-type DNA polymerase III, exonuclease domain/2P1J (*Thermotoga maritima*)	34% identical, *E* value of 1×10^{-16}

[a] Obtained with BLASTP using the PDB.

used to query the Protein Data Bank with DALILITE, the highest score ($Z = 21.6$) was observed with the Zn^{2+}-binding *Bc*ZBP protein [PDB entry 2IXD; rmsd of 2.3 Å, 24% identity (*19*)] from *B. cereus*. This deacetylase is 97% identical in sequence to the *B. anthracis* ortholog, ORF BA1557. We have recently demonstrated (*13*) that recombinant ORF BA1557 catalyzes the efficient deacetylation of GlcNAc-malate to GlcN-malate, as given in reaction II:

$$\text{GlcNAc-malate} + H_2O \rightarrow \text{GlcN-malate} + \text{OAc}^- + H^+ \qquad \text{(II)}$$

The preparative scale reaction, using GlcNAc-malate prepared by enzymatic synthesis with *Ba*BshA and purified by HPLC (see Experimental Procedures), allowed isolation of the GlcN-malate product, and deacetylation of the substrate was confirmed by ESP mass spectrometry. ORF BA1557 is the BshB GlcNAc-malate deacetylase in *B. anthracis* and is therefore designated *Ba*BshB. We have now identified the enzymatic activities, in vitro, for the *Ba*BshA glycosyltransferase and the *Ba*BshB deacetylase. Thus, from UDP-GlcNAc and L-malate precursors, these enzymes combine to produce GlcN-malate, UDP, and acetate; GlcN-malate has also been identified by HPLC analysis of cell-free extracts from *B. subtilis* (*13*), confirming this aspect of the BSH biosynthetic pathway as presented in Figure 2 for *B. anthracis*. While we have not attempted to identify GlcNAc-malate in vivo, these combined results provide very strong evidence that the biosynthetic scheme presented in Figure 2 for BshA and BshB represents the intracellular process in *B. anthracis*.

These functional assignments, as confirmed experimentally, leave the enzyme(s) responsible for the proposed ATP-dependent Cys:GlcN-malate ligase reaction (Figure 2) unidentified. The *mshC* gene product in *M. tuberculosis* is a second cysteinyl-tRNA synthetase isoform that differs from the functional CysS enzyme primarily through the absence of a 76-residue C-terminal extension that is responsible for recognition and specific binding of the tRNA^{Cys} anticodon (*46*, *47*); the Cys:GlcN-Ins ligase catalyzes the ATP-dependent formation of the amide linkage in the ultimate MSH product (+ AMP + PP_i). BLASTP analysis of the *B. anthracis* genome, however, fails to identify any second CysS isoform, and the ORF BA0089 (annotated as cysteinyl-tRNA synthetase) protein as expressed is active in the standard tRNA synthetase assay. Although deletion of the *B. subtilis yllA* locus eliminates BSH production with a concomitant increase in the intracellular level of GlcN-malate (the BshB product), the recombinant *B. subtilis* YllA and *S. aureus* CysS proteins both fail to catalyze ATP-dependent production of BSH from Cys and GlcN-malate in an in vitro assay (*13*).

Genetic Analysis of bshA and bshB Functions in B. anthracis. Passalacqua et al. (*48*) have recently demonstrated that the seven genes corresponding to BA1554−BA1560 (Ames strain) are transcribed as a single mRNA unit in *B. anthracis* Sterne (BAS1441−BAS1447); this experimental result is consistent with results obtained earlier with the operon prediction algorithm developed by Bergman et al. (*49*). Given the involvement of both BSH and CoASH in the *B. anthracis* thiol redox buffer (*2*, *10*), we note that the BA1562−BA1564 loci (*panBCD*) encoding three key enzymes in the synthesis of the CoASH precursor pantothenate (*50*) are separated by a single ORF from the *bsh* operon and have been demonstrated to be cotranscribed together with BA1565 in a second tetracistronic operon (*48*). In the event that candidate *bshC* loci might be clustered within the *bsh* operon, we analyzed the seven protein products for structural homologues of known function, using the PDB and NCBI databases. Table 1 summarizes details of the structural and functional annotations for each of the ORFs in the *bsh* and *pan* operons. Although there may be a functional linkage between BSH production and methylglyoxal synthase [ORF BA1556 (*51*)] activity (see Discussion), we find no evidence of candidate *bshC* loci in either *bsh* or *pan* operons in *B. anthracis*.

In contrast to the soil bacterium *B. subtilis*, which lacks the CoASH thiol redox buffer (*9*), the redundancy provided by the CoASH and BSH redox buffers in *B. anthracis* and *S. aureus* may provide these two pathogens with some advantage in virulence and/or survival, given the hostile environment posed by host defense mechanisms (*52*, *53*). The results described above predict that individual deletions of the *bshA* and *bshB* genes in *B. anthracis* Sterne (loci BAS1445 and BAS1444, respectively) will disrupt the BSH biosynthetic pathway at the points of GlcNAc-malate and GlcN-malate precursor production, respectively. The two mutants were prepared using the markerless deletion method developed by Janes and Stibitz (*27*) and were analyzed for low-molecular weight thiol content in parallel with wild-type *B. anthracis* Sterne and deletion mutants lacking the *cdr* and *cdr2* genes that encode *Ba*CoADR (*4*) and the chimeric CoADR-RHD protein (*9*). The major conclusions from the analytical data presented in Table 2 follow. (1) Deletion of the *bshA* locus eliminates BSH production. (2) Deletion of the *bshB* locus does not eliminate BSH production but reduces the level by 30% relative to the wild-type level. (3) BSH redox status (BSH/BSSB) strongly favors the reduced thiol in vegetative *B. anthracis* cells, and this is not affected by deletions of the *cdr* and/or *cdr2* loci. (4) The value for CoASH is higher (1.9 ± 0.4 μmol/g of dry residual weight) than that reported previously [0.87 ± 0.11

Table 2: Low-Molecular Weight Thiol Contents and Redox Ratios for *B. anthracis* Sterne Wild-Type and Mutant Strains

	thiol and disulfide contents (μmol/g of dry weight[a])			thiol and disulfide contents (μmol/g of dry weight[a])			thiol and disulfide contents (μmol/g of dry weight[a])	
strain	BSH	BSSR/0.5	redox ratio[b]	CySH	CySSR/0.5	redox ratio[b]	CoASH[c]	$S{=}SO_3^{2-}$
wild-type	1.1 ± 0.1	0.027 ± 0.004	84	0.40 ± 0.04	0.29 ± 0.04	2.8	1.9 ± 0.4	2.2 ± 0.4
Δ*bshA*	< 0.03	< 0.002	–	0.22 ± 0.06	0.43 ± 0.09	1.0	1.8 ± 0.4	2.0 ± 0.4
Δ*bshB*	0.79 ± 0.02	0.013 ± 0.002	122	0.39 ± 0.02	0.47 ± 0.056	1.7	3.0 ± 0.7	2.4 ± 0.4
Δ*cdr*	0.95 ± 0.12	0.022 ± 0.003	86	0.39 ± 0.04	0.43 ± 0.054	1.8	1.4 ± 0.3	2.2 ± 0.2
Δ*cdr2*	1.2 ± 0.06	0.03 ± 0.01	80	0.41 ± 0.02	0.40 ± 0.12	2.1	1.6 ± 0.3	2.2 ± 0.2
Δ*cdr*Δ*cdr2*	0.88 ± 0.03	0.015 ± 0.002	118	0.46 ± 0.02	0.28 ± 0.02	3.2	1.8 ± 0.1	2.5 ± 0.3

[a] Mean of triplicate determinations (*10*). [b] Expressed as thiol/disulfide (RSH/RSSR), where disulfide is estimated as half the thiol content released by dithiothreitol from an *N*-ethylmaleimide-blocked sample (*10*). [c] Includes 3′-dephospho-CoASH; the redox ratio cannot be determined with confidence because of the contribution from cleavage of acyl-CoAs by the dithiothreitol reagent (*2*, *10*).

Scheme 1: Catalytic Addition of Bacillithiol (BSH) to Fosfomycin, As Proposed for FosB

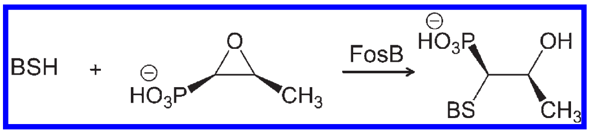

μmol/g (*2*)]; this is attributed to the different wild-type strains used in the two analyses. (5) Cys is a major low-molecular weight thiol, consistent with the recent report of Pöther et al. (*12*), for *S. aureus*. (6) Thiosulfate ($S{=}SO_3^{2-}$), a principal source of sulfur for aerobic bacteria (*54*) and the donor substrate for the sulfurtransferase rhodanese (*55*), is a major inorganic sulfur compound in *B. anthracis*.

In *B. subtilis*, the primary fosfomycin resistance determinant FosB functions as a thiol-dependent *S*-transferase that produces a thioether conjugate from the thiol and the antibiotic; until very recently, however, the enzyme had only been demonstrated to work quite poorly in vitro (*56*), with Cys as the thiol substrate. Using a zone of inhibition assay, we have recently demonstrated (*13*) that a *B. subtilis* mutant deficient in BSH is as sensitive to fosfomycin as a *fosB* mutant, leading to the conclusion that FosB is a BSH *S*-transferase. We tested the sensitivity of wild-type and Δ*bshA* mutant strains of *B. anthracis* to fosfomycin in liquid culture. While the wild-type strain grew well at 1000 μg/mL fosfomycin, the Δ*bshA* mutant did not grow at fosfomycin concentrations of ≥400 μg/mL. *B. anthracis* ORF BA4109 is annotated as the FosB protein, and we propose that this enzyme requires BSH as a cofactor for conjugation in the detoxification of fosfomycin (Scheme 1).

Our results with the Δ*bshB* mutant clearly indicate that other proteins capable of recognizing and deacetylating GlcNAc-malate are expressed in *B. anthracis*. Fadouloglou et al., in their earlier structural analysis of *Bc*ZBP (*19*), had identified ORF *Bc*3461 as a *Bc*ZBP paralog; more recently, this analysis was extended (*24*) with the identification of the BA630 (*Ba*BshB), BA425 (ORF BA3524), and BA758 (ORF BA3888) orthologs in the *B. anthracis* genome (Figure 3). ORF *Bc*3461 has now been expressed and characterized (*20*); when assayed in parallel with *Bc*ZBP, the enzyme shows a preference for $(GlcNAc)_2$ and $(GlcNAc)_3$ as deacetylase substrates. $k_{cat}/K_m(GlcNAc)_2 = 5.6 \times 10^6\ M^{-1}\ s^{-1}$, or ca. 20% of that of *Bc*ZBP. While its biological role is unclear, ORF *Bc*3461 has potent deacetylase activity. Figure 3 gives a structure-based sequence alignment for *Bc*ZBP, *Ba*BshB, ORF BA3888, ORF BA3524, and ORF *Bc*3461. While BA3888 and BA3524 are limited in their sequence similarity to *Bc*ZBP (26–28% identical), the latter protein is 95% identical in sequence to *Bc*3461; all three conserve the three Zn^{2+} protein ligands identified in *Bc*ZBP as well as the proposed active-site base and charge-relay dyad (His110/Asp112). These conserved features identify these as Zn^{2+}-dependent hydrolases;[3] Figure 3 also identifies a series of conserved insertions and deletions that distinguish the true BshB deacetylases *Bc*ZBP and *Ba*BshB from the three paralogs. These include a 10-residue insert *I1* (relative to *Bc*ZBP) after Ser45, two small inserts (one or two residues) following *Bc*ZBP Lys82 and Asp108, and two deletions *D1* and *D2* of four to six residues following Ile129 and Phe205, respectively. The *I1* insert falls within the hypermobile *Bc*ZBP active-site loop L_{46}, and the *D1* deletion falls within the L_{135} loop identified in the molecular dynamics study (*24*). Fadouloglou et al. have implicated these loops (and loop L_{185}) in active-site accessibility and substrate specificity. Further consideration of proposed ORF BA3524 and BA3888 catalytic functions is presented in a following section.

Enzymatic Characterization of BaBshA and BaBshB. Using a coupled assay, Vetting et al. (*16*) reported that the dimeric *Cg*MshA catalyzes the formation of GlcNAc-Ins-P via a sequential (ternary complex) kinetic mechanism in which the donor substrate UDP-GlcNAc almost certainly binds first. The steady-state kinetic parameters determined at pH 7.8 and 25 °C yield a K_m(UDP-GlcNAc) of 0.21 mM, a K_m(Ins-1-P) of 0.24 mM, and a k_{cat} of 12.5 s^{-1}. Structural analyses of the apoenzyme and the binary UDP complex demonstrate that nucleotide binding leads to a major rotation of the C-terminal domain relative to the N-terminal domain. k_{cat}/K_m(UDP-GlcNAc) is $6 \times 10^4\ M^{-1}\ s^{-1}$, and a superposition of the *Cg*MshA apoenzyme and UDP complex structures gives a root-mean-square deviation (rmsd) of ~11 Å, underscoring the magnitude of the conformational change in the UDP complex.

Using an HPLC assay for the UDP product, we demonstrated that the *Ba*BshA reaction was saturable with respect to both donor and acceptor substrates (Figure 4). At pH 7.5 and 37 °C, in the presence of 100 mM NaCl, the apparent kinetic parameters (at 2 mM L-malate) for UDP-GlcNAc are as follows: $K_m = 0.37$ mM, $k_{cat} = 28\ s^{-1}$, and $k_{cat}/K_m = 7.6 \times 10^4\ M^{-1}\ s^{-1}$. D-Malate, other α-hydroxy acids such as glycolate and D-lactate, and Ins-1-P gave no more than 0.5% of the activity with L-malate when assayed at 0.1 mM (Table S2 of the Supporting Information).

---

[3] Purification of the recombinant *Bc*ZBP protein employed Ni-NTA chromatography and resulted in Zn^{2+}-containing *Bc*ZBP crystals (*19*), as analyzed by both X-ray fluorescence and X-ray diffraction. Similar purification of the MshB protein (*31*), however, yielded a preparation with no Zn^{2+} and 0.82 mol of Ni^{2+} per subunit.

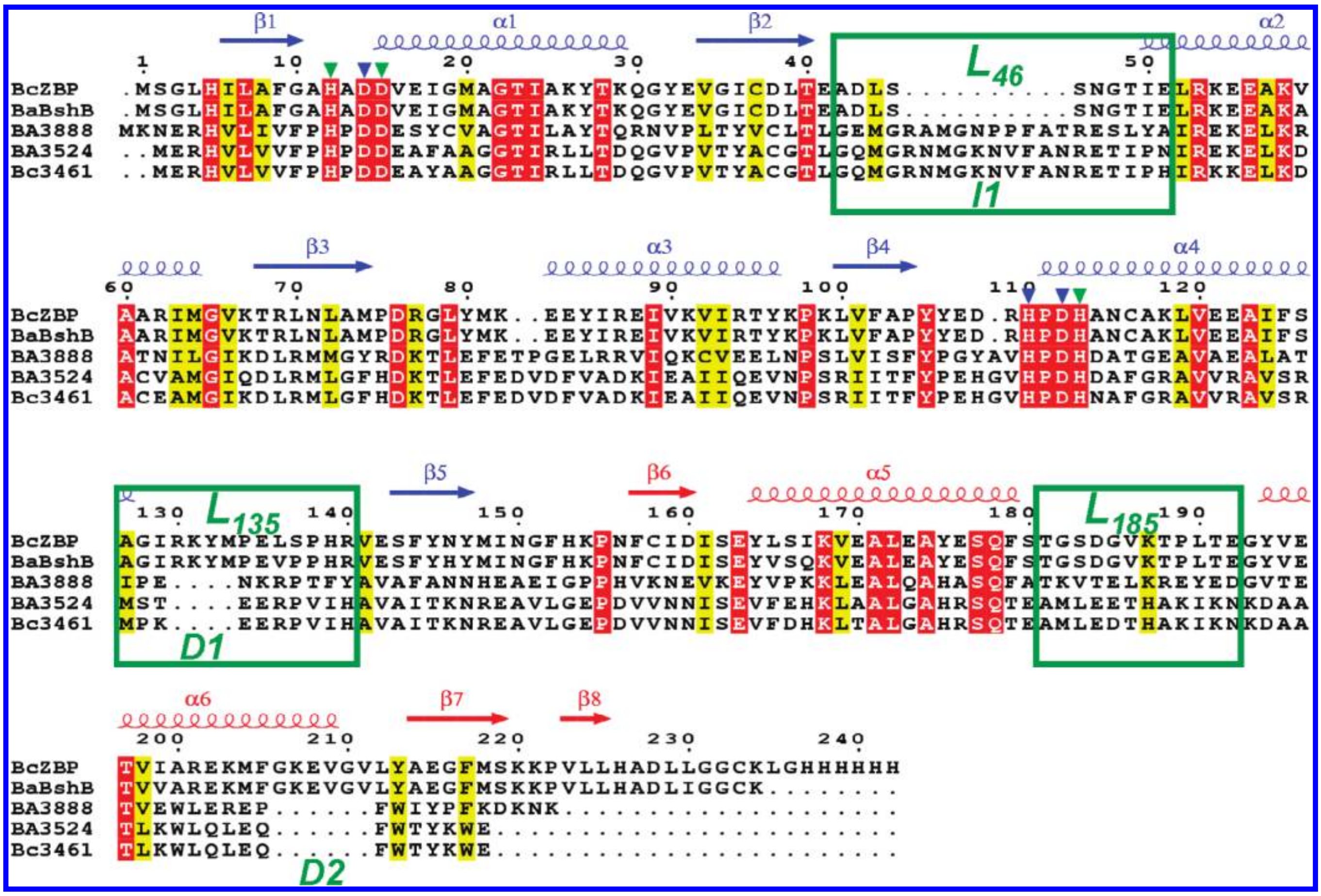

```
         1        10        20        30        40             50
BcZBP    .MSGLHILAFGAHADDVEIGMAGTIAKYTKQGYEVGICDLTEADLS..........SNGTIELRKEEAKV
BaBshB   .MSGLHILAFGAHADDVEIGMAGTIAKYTKQGYEVGICDLTEADLS..........SNGTIELRKEEAKA
BA3888   MKNERHVLIVFPHPDDESYCVAGTILAYTQRNVPLTYVCLTLGEMGRAMGNPPFATRESLYAIREKELKR
BA3524   ..MERHVLVVFPHPDDEAFAAGGTIRLLTDQGVPVTYACGTLGQMGRNMGKNVFANRETIPNIREKELKD
Bc3461   ..MERHVLVVFPHPDDEAYAAGGTIRLLTDQGVPVTYACGTLGQMGRNMGKNVFANRETIPHIRKKELKD

        60         70        80         90        100       110       120
BcZBP    AARIMGVKTRLNLAMPDRGLYMK..EEYIREIVKVIRTYKPKLVFAPYYED.RHPDHANCAKLVEEAIFS
BaBshB   AARIMGVKTRLNLAMPDRGLYMK..EEYIREIVKVIRTYKPKLVFAPYYED.RHPDHANCAKLVEEAIFS
BA3888   ATNILGIKDLRMMGYRDKTLEFETPGELRRVIQKCVEELNPSLVISFYPGYAVHPDHDATGEAVAEALAT
BA3524   ACVAMGIQDLRMLGFHDKTLEFEDVDFVADKIEAIIQEVNPSRIITFYPEHGVHPDHDAFGRAVVRAVSR
Bc3461   ACEAMGIKDLRMLGFHDKTLEFEDVDFVADKIEAIIQEVNPSRIITFYPEHGVHPDHNAFGRAVVRAVSR

          130       140       150       160       170       180       190
BcZBP    AGIRKYMPELSPHRVESFYNYMINGFHKPNFCIDISEYLSIKVEALEAYESQFSTGSDGVKTPLTEGYVE
BaBshB   AGIRKYMPEVPPHRVESFYHYMINGFHKPNFCIDISEYVSQKVEALEAYESQFSTGSDGVKTPLTEGYVE
BA3888   IPE....NKRPTFYAVAFANNHEAEIGPPHVKNEVKEYYVPKKLEALQAHASQFATKVTELKREYEDGVTE
BA3524   MST....EERPVIHAVAITKNREAVLGEPDVVNNISEVFEHKLAALGAHRSQTEAMLEETHAKIKNKDAA
Bc3461   MPK....EERPVIHAVAITKNREAVLGEPDVVNNISEVFDHKLTALGAHRSQTEAMLEDTHAKIKNKDAA

          200       210       220       230       240
BcZBP    TVIAREKMFGKEVGVLYAEGFMSKKPVLLHADLLGGCKLGHHHHHH
BaBshB   TVVAREKMFGKEVGVLYAEGFMSKKPVLLHADLIGGCK........
BA3888   TVEWLEREP......FWIYPFKDKNK....................
BA3524   TLKWLQLEQ......FWTYKWE........................
Bc3461   TLKWLQLEQ......FWTYKWE........................
```

FIGURE 3: Structure-based sequence alignment for *Bc*ZBP, *Ba*BshB, and ORFs BA3888, BA3524, and *Bc*3461. Secondary structure assignments correspond to *Bc*ZBP; red boxes represent conserved residues, and yellow boxes represent conservative substitutions. Active-site loops L_{46}, L_{135}, and L_{185} as defined for *Bc*ZBP (*24*) are indicated, as are insert *I1* and deletions *D1* and *D2* described in the text. Green and blue triangles denote ligands to the *Bc*ZBP active-site Zn^{2+} and the proposed acid−base catalyst (Asp14) and charge-relay dyad (His110/Asp112), respectively.

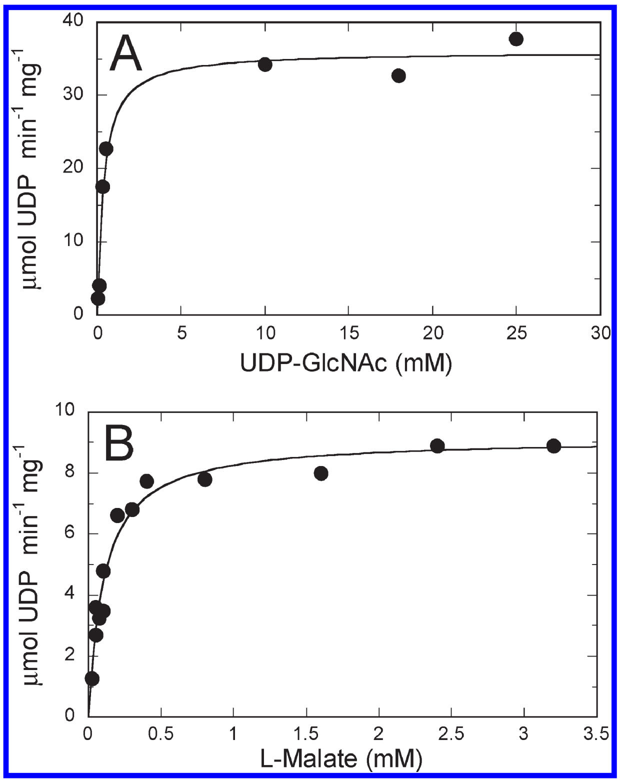

FIGURE 4: (A) UDP-GlcNAc dependence for *Ba*BshA with 2 mM L-malate. (B) L-Malate dependence with 3 mM UDP-GlcNAc.

The coupled spectrophotometric assay was then employed in an analysis of the steady-state kinetic mechanism for *Ba*BshA. As given in Figure S3 of the Supporting Information, the family of reciprocal plots obtained with varying L-malate concentrations at different fixed UDP-GlcNAc concentrations intersects below the *x*-axis. This suggests that (1) the kinetic mechanism conforms to a rapid equilibrium random bireactant system (*33*), as contrasted with an ordered system, and (2) the binding of either substrate to the free enzyme increases K^{app} for the second substrate. From the primary plot and secondary slope and intercept replots, we have determined the kinetic parameters: K_m(UDP-GlcNAc) = 0.22 mM, K_m(L-malate) = 58 μM, $k_{cat} = 15\ s^{-1}$, and α = 2.6. k_{cat}/K_m(UDP-GlcNAc) = $6.8 \times 10^4\ M^{-1}\ s^{-1}$, similar to that reported for *Cg*MshA at 25 °C.

Figure 5 gives a structure-based sequence alignment for *Cg*MshA and the three known functional BshA enzymes. An initial description of the *Ba*BshA donor substrate binding environment, based on an overlay of the apoenzyme structure with those of the UDP−2-deoxy-2-fluoroglucose complex of the GT4 glucosyltransferase WaaG and the PimA−GDP-mannose complex, identified *Ba*BshA His120, Lys211, Glu282, and Glu290 within the active site (*14*). Figure 5 demonstrates that His120 is conserved in the functional BshA enzymes; the equivalent of this His (His118) is essential for PimA activity (*57*). Lys211, interacting with the distal phosphate oxygens of UDP, and the two Glu residues, which recognize the sugar 4-OH and the ribose 2′-OH and 3′-OH groups, respectively, in the PimA

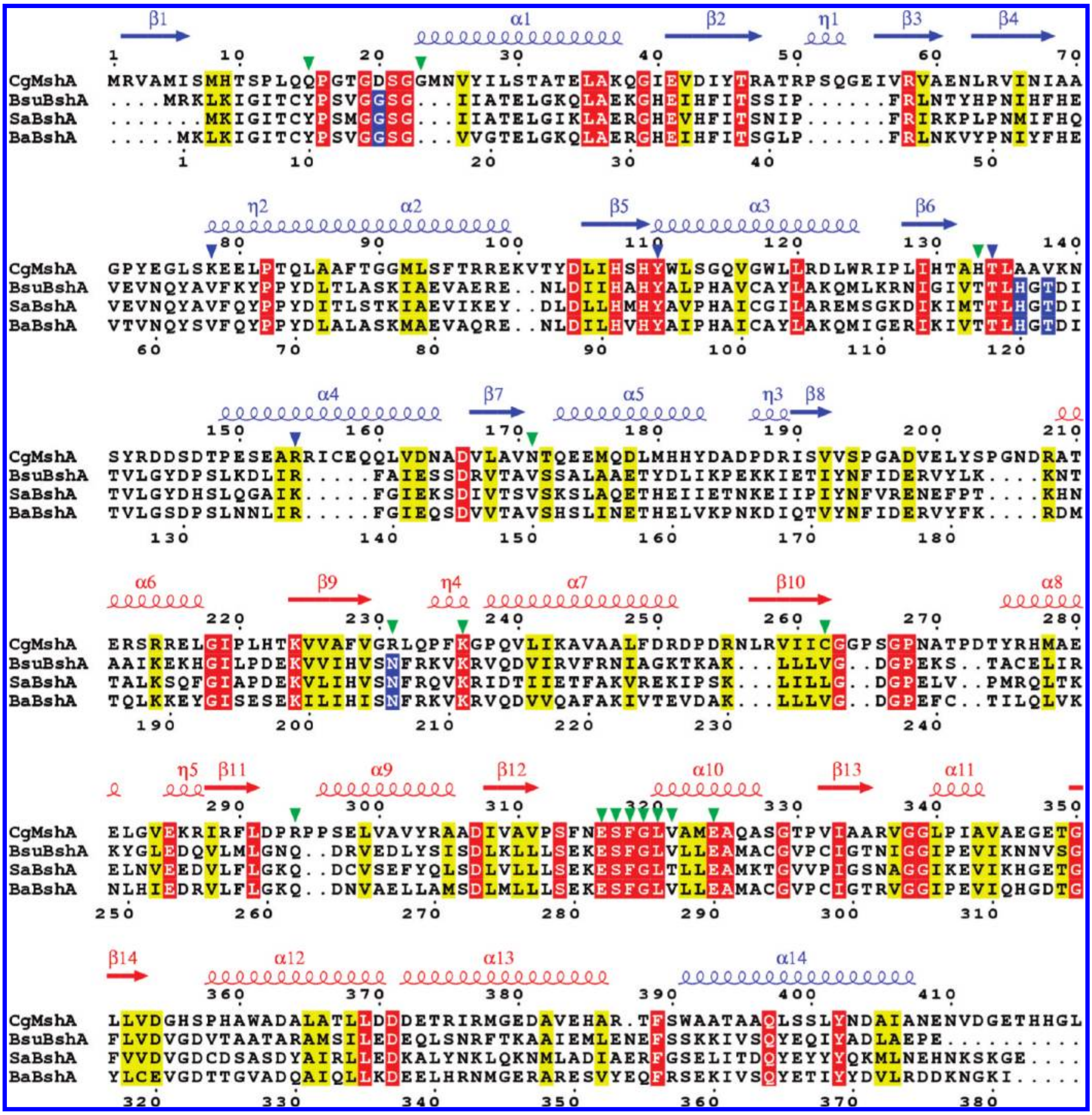

FIGURE 5: Structure-based sequence alignment for *Cg*MshA and the three known functional BshAs. Secondary structure assignments (color-coded by domain) correspond to the *Cg*MshA−UDP−Ins-1-P complex. BshA sequences correspond to *B. subtilis* {*Bsu*BshA [YpjH (*13*)]}, *S. aureus* JH9 (YP_001246887), and *B. anthracis*. *Cg*MshA and *Ba*BshA residue numbering is shown above and below the alignment, respectively. Green and blue triangles denote residues from *Cg*MshA that interact with the modeled UDP-GlcNAc substrate and with the phosphate of Ins-1-P, respectively. Blue boxes represent active-site residues conserved in BshA and thought to be important for L-malate binding and catalysis. Other details are as in Figure 3.

complex (*57*), are conserved in all four sequences. Guerin et al. demonstrated that other residues within the PimA Glu274−Ile278 signature motif, notably Ser275, Phe276, and Ile278, provide main chain hydrogen bonds to the bound mannose sugar moiety, and this motif (*Ba*BshA Glu282−Leu286, with Leu replacing Ile) is conserved in the BshA and MshA enzymes. Vetting et al. (*16*) have identified four *Cg*MshA residues (Lys78, Tyr110, Thr134, and Arg154) that coordinate the phosphate of bound Ins-1-P in the ternary complex. As represented in Figure 5, *Cg*MshA Tyr110, Thr134, and Arg154 are conserved in all three known functional BshAs, with the single exception of a conservative Arg → Lys substitution in *Sa*BshA; *Cg*MshA Lys78 is replaced with Val in the sequence alignment. When the *Ba*BshA apoenzyme is used to query the PDB database with DALILITE, the closed UDP (and UDP−Ins-1-P complex) structures for *Cg*MshA give the highest *Z* scores [∼37; rmsd = 2.4−2.5 Å (respective A chains)]. Without adjustments, the superposition represented in Figure 6 gives a clear view of the donor substrate binding environment in *Ba*BshA, as described above. In addition, the overlay demonstrates that His133 of the *Cg*MshA−UDP complex is the structural equivalent of *Ba*BshA His120 and identifies *Ba*BshA Ile204 (main chain), Asn206, Asp263, and

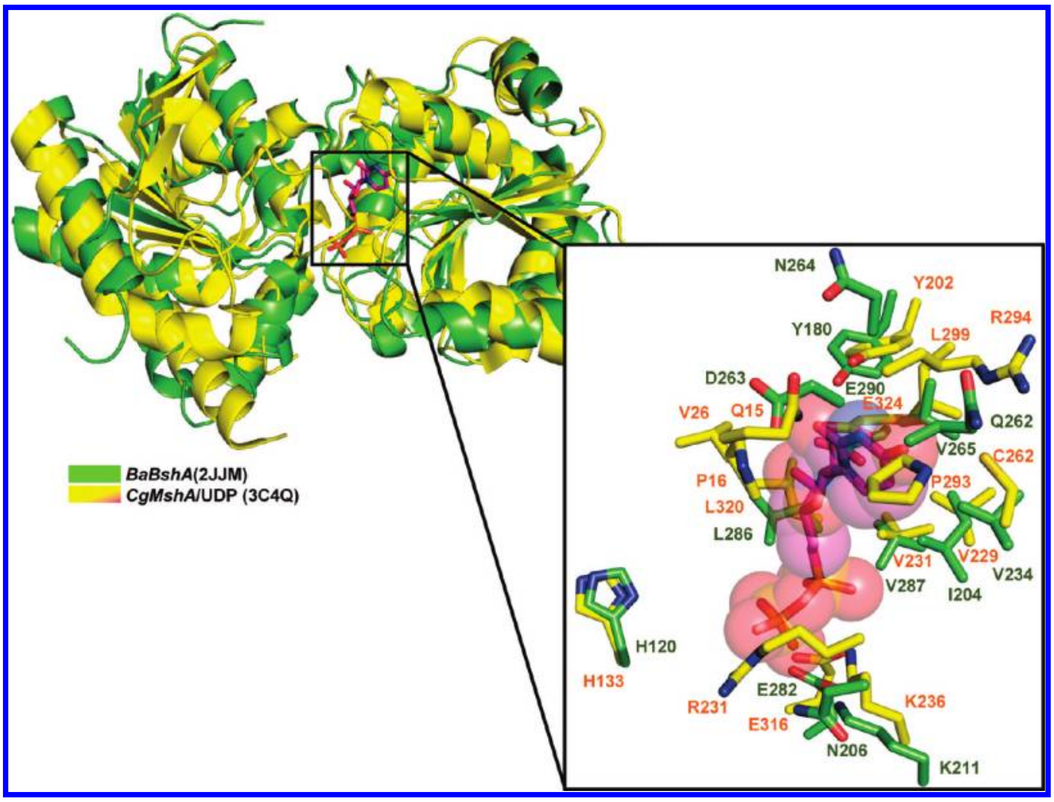

Figure 6: Monomer (left) and active-site (right) overlay for the ORF BA1558 apoenzyme and the *Cg*MshA−UDP complex. The superposition was performed using PyMOL with the respective A chains for PDB entries 2JJM (ORF BA1558) and 3C4Q (*Cg*MshA−UDP), as described in the text. ORF BA1558 and *Cg*MshA side chains (stick diagram) are color-coded by atom type, with carbon atoms colored green and yellow, respectively. Bound UDP (*Cg*MshA, with space-filling overlay rendered as 50% transparent) is included and is color-coded by atom type, with carbon atoms colored magenta. The active-site overlay depicts the bound UDP and all residues within 4 Å, as well as the *Ba*BshA His120/*Cg*MshA His133 pair.

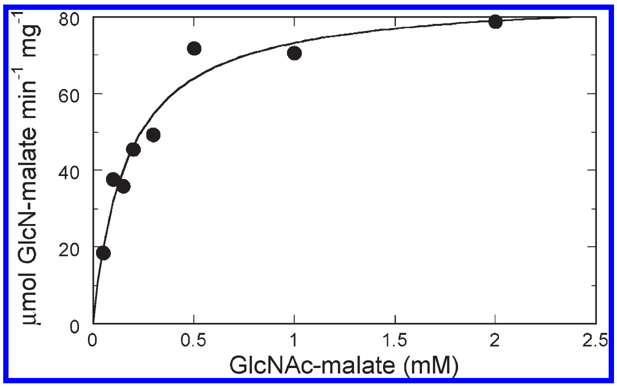

Figure 7: GlcNAc-malate dependence for *Ba*BshB.

Glu282 as likely recognition elements for the UDP pyrophosphate and for the ribose 2′-OH and uracil oxygens, respectively. There is no evidence of any conformational change upon binding of UDP to *Ba*BshA, based on the model deduced from this overlay.

The kinetic parameters for *Ba*BshB were determined using an HPLC assay for the AccQ-Tag derivative of the GlcN-malate product, as monitored by fluorescence (*13*, *31*); Figure 7 gives the resulting initial velocity plot and the fit to the Michaelis−Menten equation. At pH 7.5 and 37 °C, in the presence of 50 mM NaCl, the kinetic parameters are as follows: K_m(GlcNAc-malate) = 0.16 mM, k_{cat} = 42 s^{-1}, and k_{cat}/K_m(GlcNAc-malate) = 2.6×10^5 M^{-1} s^{-1}. We also analyzed the deacetylase activity of *Ba*BshB with GlcNAc, at a fixed concentration of 0.15 mM. The observed rate of GlcN production is $\sim 10^{-5}$ of that measured with GlcNAc-malate at the same concentration; the L-malate moiety of GlcNAc-malate is therefore a major determinant of substrate recognition and/or transition-state stabilization with *Ba*BshB. When *Ba*BshB was assayed for amidase activity with BSmB (→ CySmB + GlcN-malate), the observed rate at 0.15 mM substrate is only ca. 2×10^{-5} of that for GlcNAc-malate deacetylation.

Structural Analysis of the BaBshA−UDP−Malate Complex. To test the model for the enzyme−UDP complex described above, and in an attempt to identify the binding determinants for L-malate, we undertook a crystallographic study with the N-terminal His-tagged *Ba*BshA protein. This His tag (MGSH$_6$SSGLVPRGSHMASMTGGQQMGRGS-) differs from that for the ORF BA1558 construct (MGSSH$_6$-) analyzed by Ruane et al. (*14*), which crystallized in space group $P2_1$; there were 12 monomers organized into three tetramers within that asymmetric unit. *Ba*BshA crystals belonging to space group $P4_1$ were obtained in 0.2 M Mg(HCO$_2^-$)$_2$ containing 15% PEG 3350 with 1 mM UDP and 1 mM L-malate. The structure determined by molecular replacement using the ORF BA1558 apoenzyme coordinates has eight monomers arranged as a dimer of tetramers within the asymmetric unit (Figure 8); gel filtration analysis of the apoenzyme, in the presence of dithiothreitol, suggests that the biological unit for *Ba*BshA is the dimer. Refinement at 3.3 Å resolution led to a final model with reasonable statistics (Table 3). The final refined structure is missing the residues of the N-terminal His tag and Met1, as well as residues 11−13, 42−47, and 60−63; the short internal segments correspond closely to three of the four exposed regions in the final ORF BA1558 model (*14*). Within the *Ba*BshA asymmetric unit, the final model includes two UDP molecules,

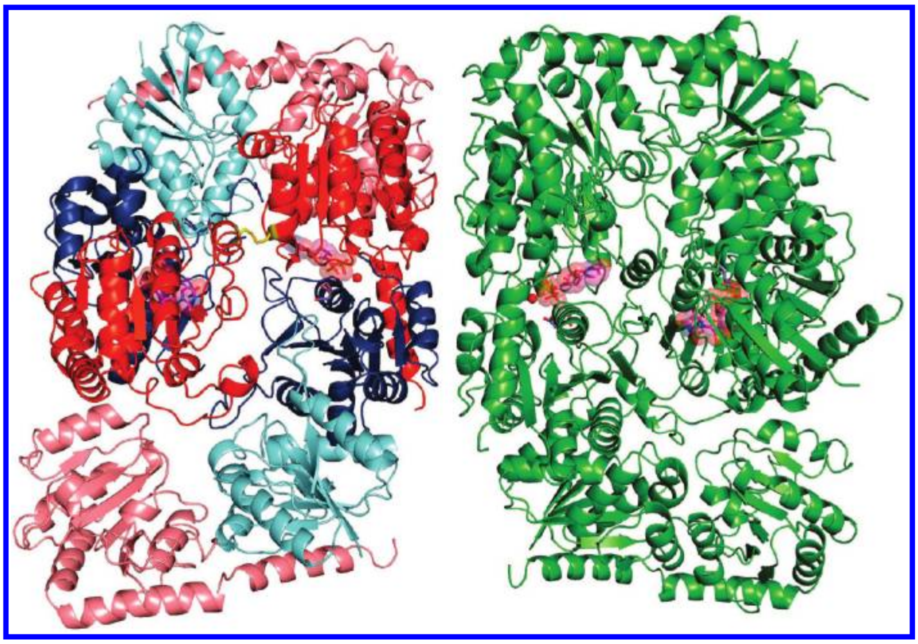

FIGURE 8: Asymmetric unit for the *Ba*BshA ternary complex. The asymmetric unit consists of a dimer of tetramers; the polypeptides of one tetramer (left) are color-coded by domain. The two polypeptides that do not contain bound substrate (cyan, N-terminal domain; salmon, C-terminal domain) are distinguished from the substrate-bound monomers (blue, N-terminal domain; red, C-terminal domain). The substrate-bound monomers are linked by the Cys241−Cys241′ disulfide (yellow). The second tetramer (right) within the asymmetric unit is colored green. For both tetramers, bound UDP molecules are color-coded as in Figure 6. Malate is color-coded by atom type, with carbon atoms colored blue and magnesium ions in the respective active sites (one per substrate-bound dimer) colored red. Stereoviews of the *Ba*BshA ternary complex, focusing on important active-site interactions, are given in Figures 10 and 11.

Table 3: Data Collection[a] and Refinement Statistics for the *Ba*BshA Complex with UDP and Malate

Data Collection	
space group	$P4_1$
cell dimensions	
a, b, c (Å)	226.3, 226.3, 75.4
α, β, γ (deg)	90, 90, 90
wavelength (Å)	1.000
resolution (Å)	226−3.31 (3.39−3.31)[b]
I/σ	12.3 (1.3)[b]
completeness (%)	99.2 (93.9)[b]
redundancy	5.7 (2.7)[b]
Refinement Statistics	
resolution (Å)	226−3.31
no. of reflections	54419
R_{work}	0.229
R_{free}	0.259
no. of molecules per asymmetric unit (AU)	8
no. of amino acid residues per AU	2961
no. of waters per AU	288
average B factor	69.7
stereochemical ideality	
bond length rmsd (Å)	0.009
bond angle rmsd (deg)	1.97
φ and ψ preferred (%)	93.7
φ and ψ allowed (%)	5.90
φ and ψ outliers (%)	0.40
PDB entry	3MBO

[a] Collected at SER-CAT beamline BM-22 of the Advanced Photon Source. [b] Numbers in parentheses represent data for the highest-resolution shell.

two malates, and one Mg^{2+} per tetramer; Vetting et al. (*16*) reported that Ins-1-P soaks of *Cg*MshA−UDP crystals resulted in a complex with two UDP molecules, two Mg^{2+} ions, and only one Ins-1-P per dimeric asymmetric unit. The dimeric (substrate-bound) unit of the *Ba*BshA−UDP−malate complex gives an overall C_α rmsd of 1.1 Å for 371 atoms when compared with the corresponding dimeric unit of the ORF BA1558 apoenzyme (Figure 9). In addition, the two subunits per tetramer that are complexed with UDP and malate are covalently linked via an intersubunit Cys241−Cys241′ disulfide (Figure 8); this disulfide is not observed with the complementary unbound subunits within that tetramer, which appear to reflect crystal packing. Focusing on one of the subunits containing bound UDP and malate, Figure 10 gives a final composite omit $F_o - F_c$ map in the vicinity of the substrates, together with the refined model. Considering the 3.3 Å resolution of the *Ba*BshA complex, we have also worked with the possibility of modeling glycerol in two conformations as an alternative to malate. Two conformations of glycerol could be modeled into the density; however, after refinement, additional positive density appears. Upon placement of malate in the electron density, no additional F_o-F_c density appears.

Bacillithiol is only the second malyl glycoside reported in the literature to date (*10*, *58*), and the interactions and specificity determinants for L-malate recognition are of significant interest, particularly given the recent report that L-malate is a second preferred carbon source in *B. subtilis* (*59*), strongly contributing to repression of the uptake of alternate substrates. An overlay of the *Cg*MshA−UDP−Ins-1-P and *Ba*BshA−UDP−malate complexes (not shown) demonstrates that the positioning and geometry of the Ins-1-P 3-OH and malate 2-OH groups, relative to the distal phosphates of the respective UDPs, are similar. Neither malate carboxylate is close to the position of the Ins-1-P phosphate, however. Although this interpretation is limited by the 3.3 Å resolution of the *Ba*BshA complex, it is consistent with a chemical mechanism [Scheme 2 (*16*, *60*)] involving nucleophilic attack by the malate 2-OH group on the anomeric carbon of UDP-GlcNAc.

The superposition of the two complexes also demonstrates that two residues in the *Cg*MshA phosphate coordination site, Tyr110 and Thr134 (see Figure 5), are structurally conserved in *Ba*BshA. BshA Val64 does occupy the same approximate position as MshA Lys78, but the respective Arg138 and Arg154 residues are not equivalent. Figure 11 gives a stereo representation of the *Ba*BshA−UDP−malate active site, focusing on important polar interactions with both malate and UDP. In particular, this analysis identifies Thr122 OH, Asn206 $N_{\delta2}$ and $O_{\delta1}$, and a distal phosphate oxygen (O1B) of UDP as ligands to the malate C1-carboxylate. The substrate C2-OH group interacts with Gly15 N and with both O1B and O2B atoms of the uridine pyrophosphate, and Ser16 O stabilizes the C4-carboxylate. All four *Ba*BshA residues are conserved in the other known functional BshA enzymes (Figure 5). It has previously been proposed (*61*) that an active-site His functions in glycogen phosphorylase and related glycosyltransferases to stabilize an oxocarbenium transition state (e.g., via interaction with His377 O in glycogen phosphorylase) such as that considered for *Cg*MshA. This is thought to be especially important for those GT enzymes operating with negatively charged (e.g., malate and Ins-1-P) acceptor substrates (*61*), and the conservation of His120 in the *Ba*BshA catalytic center appears to be an important factor in this regard.

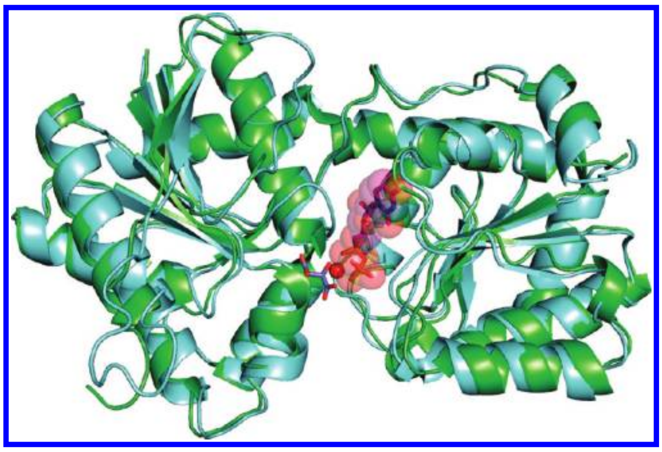

FIGURE 9: Superposition of the *Ba*BshA−UDP−malate complex (chain A, cyan) with an apoenzyme (PDB entry 2JJM) monomer (green). An overlay with the respective dimers gives a rmsd of 1.1 Å for 371 C_α atoms. Bound UDP, malate, and magnesium ion are color-coded as in Figure 8.

With regard to UDP binding, the structure of the *Ba*BshA ternary complex confirms several aspects of the model deduced from the overlay described in Figure 6. The very favorable comparison of apoenzyme and ternary complex structures (Figure 9) demonstrates that there is no major conformational change when the substrate binds to *Ba*BshA.

DISCUSSION

BaBshA Structure and Kinetics. In this work, we have defined the functions of ORF BA1558, previously annotated as a glycosyltransferase, group 1 family protein, and ORF BA1557, previously annotated as a hypothetical protein, as the *N*-acetyl-α-D-glucosaminyl L-malate synthase (*Ba*BshA) and deacetylase (*Ba*BshB), respectively. The GlcNAc-malate product of *Ba*BshA has been confirmed by ^{1}H and ^{13}C NMR and by high-resolution mass spectrometry; deacetylation by *Ba*BshB gives GlcN-malate, as confirmed by ESP mass spectrometry. The kinetic parameters have been determined for both enzymes. *Ba*BshA is specific for L-malate and does not recognize either D-malate or other α-hydroxy acids as acceptor substrates. *Ba*BshA appears to follow a rapid equilibrium random bireactant mechanism in which the binding of either substrate increases K^{app} for the second substrate (*33*). Vetting et al. (*16*) reported that *Cg*MshA followed a sequential mechanism in which UDP-GlcNAc was proposed to bind first, i.e., as in a rapid equilibrium ordered bireactant scheme. However, Segel has shown that the family of reciprocal

Scheme 2: Possible Oxocarbenium Ion-like Transition State for the Glycosyltransferase Reaction of *Ba*BshA (adapted from refs *16* and *60*)

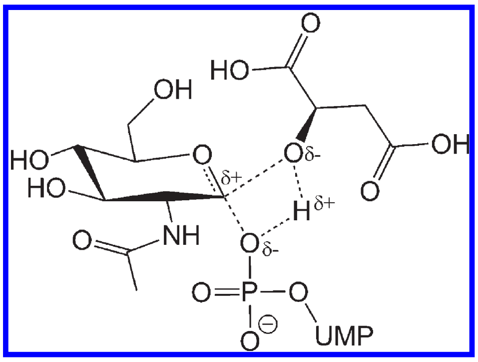

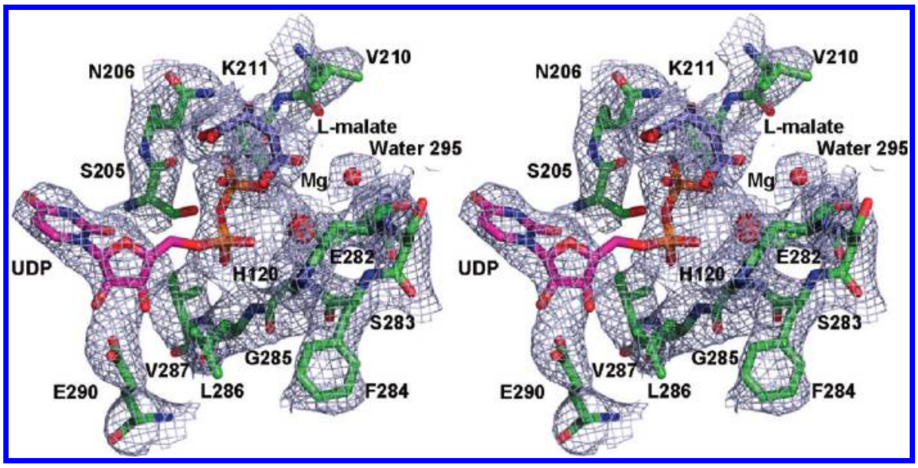

FIGURE 10: Stereoview of the *Ba*BshA−UDP−malate complex, focusing on the active site. The refined model includes bound UDP and malate, Mg^{2+}, one water molecule (water 295), and protein segments corresponding to His120, Ser205, Asn206, Val210, Lys211, Glu282−Val287, and Glu290. A composite omit $F_o - F_c$ map is shown contoured at 1.2σ. All atoms are color-coded as in Figure 8 except for *Ba*BshA C_α and side chain carbon atoms, which are colored green.

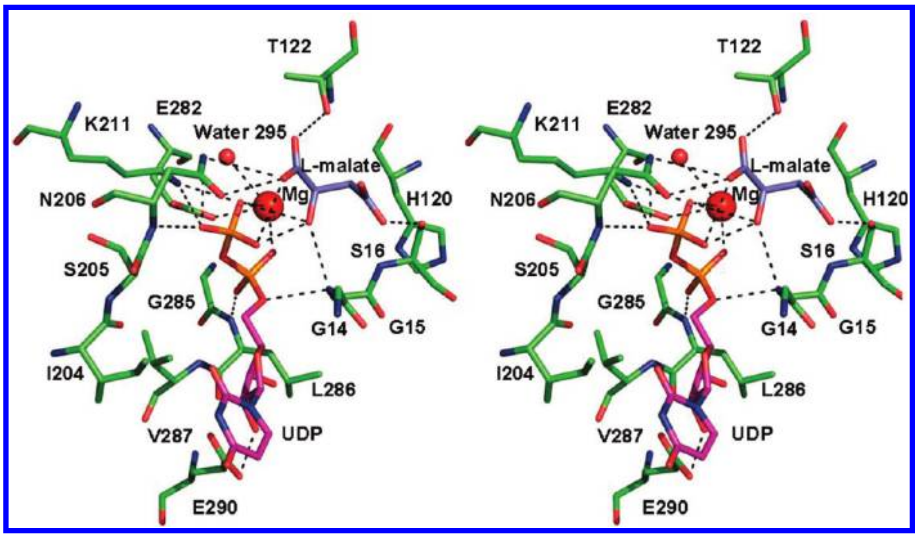

FIGURE 11: Stereo representation of the *Ba*BshA ternary complex, focusing on important polar interactions with UDP and malate. Hydrogen bonding interactions (black dashed lines) are shown for bound UDP, malate, Mg^{2+}, and water 295. All atoms are color-coded as in Figure 10.

plots (1/*v* vs 1/[Acc], at several fixed Don concentrations) for such an ordered sequential mechanism intersects on the *y*-axis, in the case where substrate A (e.g., UDP-GlcNAc) binds first (*33*). An examination of the data (*16*) indicates, in contrast, that reciprocal plots of 1/*v* versus 1/[Ins-1-P] for *Cg*MshA intersect in the second quadrant, very close to the *x*-axis. We suggest that *Ba*BshA and *Cg*MshA both follow rapid equilibrium random bireactant mechanisms; they differ primarily in the fact that $\alpha \sim 1$ for *Cg*MshA. While binding of either substrate to *Ba*BshA has the effect of increasing K^{app} for the second substrate ($\alpha = 2.6$), this interpretation does not apply to *Cg*MshA.

The k_{cat}/K_m(UDP-GlcNAc) values of 6.8×10^4 M^{-1} s^{-1} (37 °C) and 6×10^4 M^{-1} s^{-1} (25 °C) correspond to free energies of activation [$\Delta G_T^{\ddagger}$ (*62*)] of 11.3 and 10.9 kcal/mol, respectively. This quantitative similarity is significant, in that Vetting et al. (*16*) have reported a large conformational change between the *Cg*MshA apoenzyme and UDP complex. Apoenzyme crystals were prepared with an N-terminal His-tagged protein and were of space group $P3_1$, while crystals of the complex were prepared with a C-terminal His-tagged protein and were of space group *I*422. While a crystallographic argument has been presented against the possibility that the apoenzyme conformation does not represent the functional enzyme, this remains an open question. In particular, searches using the *Cg*MshA apoenzyme with the SSM server yielded no significant structural homologues among the GT-B fold family. There is no major conformational change on UDP binding to *Ba*BshA; the possibility of a conformationally distinct *Ba*BshA−UDP-GlcNAc complex also appears unlikely, as the superposition of the *Ba*BshA apoenzyme with the monomeric PimA−GDP-mannose structure reveals similar conformational states ($Z = 33.6$, and rmsd = 3.0 Å). In view of the K_m(UDP-GlcNAc) value of 0.22 mM for *Ba*BshA, the intracellular concentration of ca. 2.4 mM reported for *B. megaterium* (*63*) predicts that ca. 8% of the enzyme is present in the apo form in the in vivo steady state. With respect to the *Ba*BshA complex, crystal packing stabilizes a closed tetrameric protein form [two UDP molecules and two malates per tetramer (Figure 8)] in which bound UDP is solvent inaccessible. Similarly, Vetting et al. showed that crystals of the dimeric *Cg*MshA−UDP complex, when soaked with high concentrations of UDP-GlcNAc, do not exchange bound UDP (*16*).

Bioinformatics of the B. anthracis bsh and pan Operons. Using a transposon-site hybridization assay protocol, Day et al. (*64*) concluded (without the benefit of the functional assignments presented in this work) that the *bshA* and *panC* genes, as well as BA1559 [*pcnB* (Table 1)], were individually required for optimal growth, sporulation, or germination in *B. anthracis* strain ΔAmes. As we have demonstrated that deletion of the *bshA* locus in *B. anthracis* Sterne eliminates BSH production, this suggests that BSH is important for one or more of these aspects of the life cycle. In this context, we have recently demonstrated that the *B. subtilis bshA* mutant sporulates with an efficiency that is ~1% of that of the wild-type strain (*13*). In their transcriptional profiling of the *B. anthracis* life cycle, in which five distinct temporal waves of gene expression were identified from germination through sporulation, Bergman et al. (*65*) showed that the *bshA* and *bshB* genes encoding the first two enzymes in the BSH biosynthetic pathway are upregulated together in waves II and III; the *panBCD* genes are upregulated in wave V of the germination→sporulation cycle. *panB* and *panC* are also upregulated between 1 and 2 h postinfection within host macrophages (*52*).

We have described the gene products for all seven loci in the *bsh* operon, which is upregulated during that part of the life cycle corresponding to early outgrowth to rapid growth (*65*). Aside from the GlcNAc-malate synthase and deacetylase enzymes, we find no evidence of coding sequences that provide for the enzymatic conversion of GlcN-malate to BSH. In connection with the demonstration that BSH is important for fosfomycin resistance in *B. anthracis*, the coexpression of the *mgsA* gene encoding methylglyoxal synthase is of interest. Methylglyoxal is cytotoxic at millimolar concentrations and is also mutagenic (*51*). Still, many bacteria produce methylglyoxal synthase, with a functional implication as a bypass of glycolysis active under conditions of P_i starvation. In most microorganisms, methylglyoxal is detoxified via GSH-dependent conversion to D-lactate; however, we have demonstrated that GSH is absent in *B. anthracis* (*2*). Both methylglyoxal (*51*) and fosfomycin (*66*) are potent C_3-electrophiles known to react with GSH, and our evidence strongly suggests that BSH is the cofactor for FosB in *B. anthracis*. We have recently demonstrated, using a zone of inhibition assay, that a *B. subtilis bshA* mutant has a significantly increased sensitivity to methylglyoxal (*13*). We conclude that

BSH may also be the cofactor for an *S*-transferase reaction converting methylglyoxal to lactoyl-bacillithiol [$CH_3CHOHCO$-$SCH_2CH(NH_3^+)CO$-NGlc-malate]. A possible fate of these BSH conjugates is discussed below.

BaBshB Structure, Function, and Genetics. As indicated previously, BshB is both a structural and functional homologue of *M. tuberculosis* MshB; when assayed in parallel with synthetic GlcNAc-Ins, however, MshB gives a k_{cat} of only 0.49 s^{-1} (*31*), with a k_{cat}/K_m(GlcNAc-Ins) of 1.44×10^3 M^{-1} s^{-1}. Both values are ca. 1% of the respective parameters with *Ba*BshB (acting on GlcNAc-malate as the substrate). The difference in BshB and MshB catalytic efficiencies is approximately that required by rapidly dividing cells to maintain stable levels of BSH and MSH, respectively, given the 50-fold difference in generation times for *B. anthracis* and *M. tuberculosis* (0.5 and 24 h). We have shown that the *B. anthracis* Δ*bshB* mutant produces BSH at ca. 70% of the wild-type level, and this has been attributed to an overlapping substrate specificity for two *Ba*BshB paralogs, ORFs BA3524 and BA3888. In the closely related *B. cereus* 14579, the ORF *Bc*3461 ortholog of BA3524 has been demonstrated (*20*) to catalyze deacetylation of both $(GlcNAc)_2$ and $(GlcNAc)_3$, and we propose that this enzyme and *Bc*ZBP similarly have overlapping specificities for GlcNAc-malate deacetylation in *B. cereus*. A *Bc*ZBP-deficient mutant would still be expected to produce significant BSH, through the action of ORF *Bc*3461.

The substrate specificity of the MshB deacetylase overlaps that of the *M. tuberculosis* mycothiol *S*-conjugate amidase (Mca), which functions in the MSH-dependent detoxification of thiol-reactive drugs and metabolites by cleaving the Cys−GlcN amide bond of the *S*-conjugate to give AcCySR and GlcN-Ins. The optimal amidase substrate for Mca is MSmB, yielding AcCySmB and GlcN-Ins; $k_{cat}/K_m = 9 \times 10^4$ M^{-1} s^{-1} at 37 °C (*23*), and MshB catalyzes amide cleavage with this substrate, though with a k_{cat}/K_m of 460 M^{-1} s^{-1} (*31*), less than 1% of the value observed with Mca. The *M. tuberculosis* Rv1170 mutant deficient in MshB continues to produce MSH at ca. 20% of the wild-type level (*67*), and this has been attributed to the weak deacetylase activity observed with purified Mca in vitro for GlcNAc-Ins [k_{cat}/K_m = 0.3 M^{-1} s^{-1} (*23*)], ca. 10^{-4} of that of MshB (see above). In addition to providing for GlcNAc-malate deacetylation in the absence of BshB (see above), ORFs *Bc*3461, BA3524, and BA3888 may function primarily as paralogs of Mca that catalyze bacillithiol *S*-conjugate amidase reactions related to xenobiotic detoxification. The *S*-conjugates of fosfomycin and methylglyoxal described above represent two potential substrates (Scheme 3). The charged GlcN-malate product of the amidase reaction can be recycled for BSH synthesis, and a number of AcCySR products from the analogous amidase reactions with mycothiol *S*-conjugates are known to be lost from the cell (*44*, *45*). Rukmana et al. (*68*) have recently reported that the Spx regulon is induced in *B. subtilis* cells challenged by the antibiotics enduracin and bacitracin, suggesting that disulfide stress is occurring under these conditions, but the Spx regulatory system appears to be independent of BSH (*13*).

Nature and Influence of Low-Molecular Weight Thiols as Redox Buffers in B. anthracis. Bacterial growth and proliferation, especially during infection of the host, often involve a hostile environment (*52*, *53*) that challenges the defensive mechanisms of the pathogen (e.g., *B. anthracis* or *S. aureus*). Among the physiological mechanisms for maintaining thiol−disulfide redox homeostasis are the important functions of thiols such as GSH (*69*, *70*) and MSH (*44*, *45*). *B. anthracis* (*2*), *S. aureus* (*3*), and *B. megaterium* (*11*) are among a number of Gram-positive bacteria that lack both of these thiols. It is clear from several studies, perhaps most closely associated with the Beckwith laboratory (*69*, *70*), that redundancy in these systems is the rule, particularly in *E. coli*; mutants lacking either TrxR or glutathione reductase grow normally (*70*, *71*).

Scheme 3: Bacillithiol *S*-Conjugate Amidase (Bca) Reaction Proposed for ORFs *Bc*3461, BA3524, and BA3888[a]

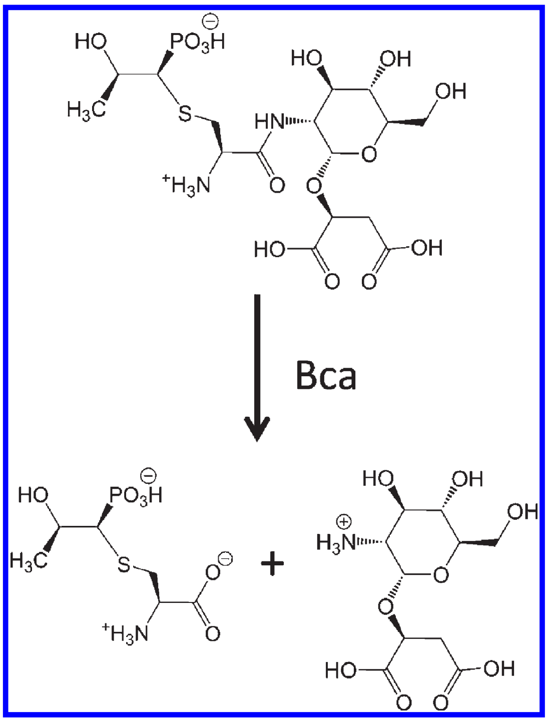

[a]The *S*-conjugate of fosfomycin (Scheme 1) is taken as the substrate.

Figure 12 gives our working scheme for cytoplasmic disulfide reducing and oxidizing pathways in our model Gram-positive pathogen, *B. anthracis*; the same system or a very similar system applies in *S. aureus* and in the soil bacterium *B. megaterium*. The three branches include CoASH/CoADR, Trx/TrxR, and bacillithiol (BSH). The recent work of Pöther et al. (*12*) indicates that cysteine (CySH) represents a fourth branch in *S. aureus*, accounting for most protein (mixed) disulfide formation during diamide stress. While a specific bacillithiol disulfide reductase has not been identified, the BSH/BSSB redox status is very reduced (redox ratio of 84 vs 2.8 for CySH/CySSR) in vegetative *B. anthracis* cells (Table 2); this ratio is unchanged in the Δ*cdr* and Δ*cdr2* mutants, and neither CoADR nor CoADR-RHD is a reductant of oxidized bacillithiol (BSSB). There is, however, no direct evidence of whether the *B. anthracis* Trx/TrxR system might reduce BSSB. In both *Arabidopsis* (*72*) and *Drosophila* (*73*), for example, the Trx/TrxR system either constitutes a functional backup or substitutes for glutathione reductase. In *E. coli*, the Grx-SSG reductase activity of AhpC* maintains the reduced GSH pool at essentially wild-type levels in Δ*gor*Δ*trxB* strains (*70*).

We recently demonstrated (*8*) that the *B. anthracis cysK-1* locus encoding cysteine synthase A is part of the tricistronic *coaX* operon that also encodes the type III pantothenate kinase. The *B. anthracis* pathway from pantothenate to CoASH (Figure 13), as well as the components of the de novo pantothenate biosynthetic pathway [including the *panBCD* genes of the *pan* operon

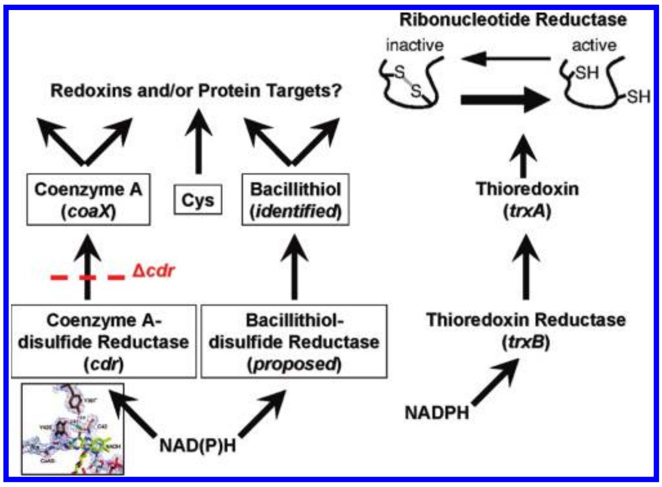

FIGURE 12: Cytoplasmic thiol redox pathways in *B. anthracis*. Structural genes are identified in parentheses beneath the proteins; the *coaX* gene encodes the type III pantothenate kinase that catalyzes the first step in CoASH biosynthesis. Results with the Δ*cdr* mutant are described in Table 2 and in the text. TrxA appears to reduce ribonucleotide reductase in *B. subtilis*, but this is still under investigation. The thumbnail representation of the *B. anthracis* CoADR active-site structure is adapted from Figure 5 of ref *4*.

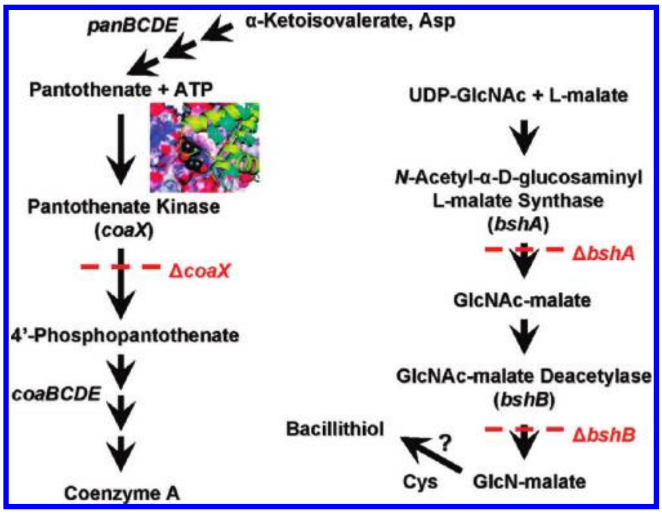

FIGURE 13: CoASH and BSH biosynthetic pathways in *B. anthracis*. Structural genes are identified in parentheses beneath the proteins; the properties of the Δ*bshA* and Δ*bshB* mutants are described in Table 2 and in the text. The properties of a conditional *coaX* mutant have been reported previously (*8*). The thumbnail representation of the *B. anthracis* pantothenate kinase active-site structure is adapted from Figure 7 of ref *2*.

(Table 1)], has now been established (*2*, *74*). In this work, we describe the first two steps in BSH biosynthesis for *B. anthracis* and the effects of deleting the respective genes on BSH production. While the identification of the proposed Cys:GlcN-malate ligase, the biological functions of the *B. subtilis* YllA and ORF BA3524 proteins, and the description of the reductase(s) that maintain the reduced status of BSH in vegetative *B. anthracis* cells remain as priority goals, the materials necessary for genetic analysis of the relative roles of the CoASH/CoADR and BSH systems in both intracellular thiol−disulfide redox homeostasis and in virulence are presently being exploited.

ACKNOWLEDGMENT

We gratefully acknowledge Dr. Robert Fahey, who first identified bacillithiol and led the structure determination, for his generous support and for many very helpful discussions. We thank Dr. Philip Hanna for hosting one of us (C.P.) in his laboratory and contributing to the construction of mutant strains, Dr. James La Clair for help with NMR work, and Ms. Kelly Lo and Mr. Austin Dosch for technical assistance.

SUPPORTING INFORMATION AVAILABLE

Figures S1 and S2 depicting preparative-scale production and NMR characterization of GlcNAc-malate, respectively, Figure S3 providing reciprocal plots of *Ba*BshA activity, and Tables S1 and S2 providing the primer sequences used in the study and describing the acceptor substrate specificity for *Ba*BshA, respectively. This material is available free of charge via the Internet at http://pubs.acs.org.

REFERENCES

1. Zuber, P. (2009) Management of oxidative stress in *Bacillus*. *Annu. Rev. Microbiol. 63*, 575–597.
2. Nicely, N. I., Parsonage, D., Paige, C., Newton, G. L., Fahey, R. C., Leonardi, R., Jackowski, S., Mallett, T. C., and Claiborne, A. (2007) Structure of the type III pantothenate kinase from *Bacillus anthracis* at 2.0 Å resolution: Implications for coenzyme A-dependent redox biology. *Biochemistry 46*, 3234–3245.
3. delCardayre, S. B., Stock, K. P., Newton, G. L., Fahey, R. C., and Davies, J. E. (1998) Coenzyme A disulfide reductase, the primary low molecular weight disulfide reductase from *Staphylococcus aureus*. Purification and characterization of the native enzyme. *J. Biol. Chem. 273*, 5744–5751.
4. Wallen, J. R., Paige, C., Mallett, T. C., Karplus, P. A., and Claiborne, A. (2008) Pyridine nucleotide complexes with *Bacillus anthracis* coenzyme A-disulfide reductase: A structural analysis of dual NAD(P)H specificity. *Biochemistry 47*, 5182–5193.
5. delCardayre, S. B., and Davies, J. E. (1998) *Staphylococcus aureus* coenzyme A disulfide reductase, a new subfamily of pyridine nucleotide-disulfide oxidoreductase. Sequence, expression, and analysis of *cdr*. *J. Biol. Chem. 273*, 5752–5757.
6. Luba, J., Charrier, V., and Claiborne, A. (1999) Coenzyme A-disulfide reductase from *Staphylococcus aureus*: Evidence for asymmetric behavior on interaction with pyridine nucleotides. *Biochemistry 38*, 2725–2737.
7. Mallett, T. C., Wallen, J. R., Karplus, P. A., Sakai, H., Tsukihara, T., and Claiborne, A. (2006) Structure of coenzyme A-disulfide reductase from *Staphylococcus aureus* at 1.54 Å resolution. *Biochemistry 45*, 11278–11289.
8. Paige, C., Reid, S. D., Hanna, P. C., and Claiborne, A. (2008) The type III pantothenate kinase encoded by *coaX* is essential for growth of *Bacillus anthracis*. *J. Bacteriol. 190*, 6271–6275.
9. Wallen, J. R., Mallett, T. C., Boles, W., Parsonage, D., Furdui, C. M., Karplus, P. A., and Claiborne, A. (2009) Crystal structure and catalytic properties of *Bacillus anthracis* CoADR-RHD: Implications for flavin-linked sulfur trafficking. *Biochemistry 48*, 9650–9667.
10. Newton, G. L., Rawat, M., La Clair, J. J., Jothivasan, V. K., Budiarto, T., Hamilton, C. J., Claiborne, A., Helmann, J. D., and Fahey, R. C. (2009) Bacillithiol is an antioxidant thiol produced in *Bacilli*. *Nat. Chem. Biol. 5*, 625–627.
11. Swerdlow, R. D., and Setlow, P. (1983) Purification and characterization of a *Bacillus megaterium* disulfide reductase specific for disulfides containing pantethine 4′,4″-diphosphate. *J. Bacteriol. 153*, 475–484.
12. Pöther, D.-C., Liebeke, M., Hochgräfe, F., Antelmann, H., Becher, D., Lalk, M., Lindequist, U., Borovok, I., Cohen, G., Aharonowitz, Y., and Hecker, M. (2009) Diamide triggers mainly *S*-thiolations in the cytoplasmic proteomes of *Bacillus subtilis* and *Staphylococcus aureus*. *J. Bacteriol. 191*, 7520–7530.
13. Gaballa, A., Newton, G. L., Antelmann, H., Parsonage, D., Upton, H., Rawat, M., Claiborne, A., Fahey, R. C., and Helmann, J. D. (2010) Biosynthesis and functions of bacillithiol, a major low-molecular-weight thiol in *Bacilli*. *Proc. Natl. Acad. Sci. U.S.A. 107*, 6482–6486.
14. Ruane, K. M., Davies, G. J., and Martinez-Fleites, C. (2008) Crystal structure of a family GT4 glycosyltransferase from *Bacillus anthracis* ORF BA1558. *Proteins 73*, 784–787.
15. Newton, G. L., Ta, P., Bzymek, K. P., and Fahey, R. C. (2006) Biochemistry of the initial steps of mycothiol biosynthesis. *J. Biol. Chem. 281*, 33910–33920.

16. Vetting, M. W., Frantom, P. A., and Blanchard, J. S. (2008) Structural and enzymatic analysis of MshA from *Corynebacterium glutamicum*: Substrate-assisted catalysis. *J. Biol. Chem. 283*, 15834–15844.
17. Franco, O. L., and Rigden, D. J. (2003) Fold recognition analysis of glycosyltransferase families: Further members of structural superfamilies. *Glycobiology 13*, 707–712.
18. Cantarel, B. L., Coutinho, P. M., Rancurel, C., Bernard, T., Lombard, V., and Henrissat, B. (2009) The Carbohydrate-Active enZymes database (CAZy): An expert resource for glycogenomics. *Nucleic Acids Res. 37*, D233–D238.
19. Fadouloglou, V. E., Deli, A., Glykos, N. M., Psylinakis, E., Bouriotis, V., and Kokkinidis, M. (2007) Crystal structure of the *Bc*ZBP, a zinc-binding protein from *Bacillus cereus*. *FEBS J. 274*, 3044–3054.
20. Deli, A., Koutsioulis, D., Fadouloglou, V. E., Spiliotopoulou, P., Balomenou, S., Arnaouteli, S., Tzanodaskalaki, M., Mavromatis, K., Kokkinidis, M., and Bouriotis, V. (2010) LmbE proteins from *Bacillus cereus* are de-*N*-acetylases with broad substrate specificity and are highly similar to proteins in *Bacillus anthracis*. *FEBS J. 277*, 2740–2753.
21. Watanabe, R., Ohishi, K., Maeda, Y., Nakamura, N., and Kinoshita, T. (1999) Mammalian PIG-L and its yeast homologue Gpi12p are *N*-acetylglucosaminylphosphatidylinositol de-N-acetylases essential in glycosylphosphatidylinositol biosynthesis. *Biochem. J. 339*, 185–192.
22. Maynes, J. T., Garen, C., Cherney, M. M., Newton, G. L., Arad, D., Av-Gay, Y., Fahey, R. C., and James, M. N. G. (2003) The crystal structure of 1-D-*myo*-inositol 2-acetamido-2-deoxy-α-D-glucopyranoside deacetylase (MshB) from *Mycobacterium tuberculosis* reveals a zinc hydrolase with a lactate dehydrogenase fold. *J. Biol. Chem. 278*, 47166–47170.
23. Steffek, M., Newton, G. L., Av-Gay, Y., and Fahey, R. C. (2003) Characterization of *Mycobacterium tuberculosis* mycothiol *S*-conjugate amidase. *Biochemistry 42*, 12067–12076.
24. Fadouloglou, V. E., Stavrakoudis, A., Bouriotis, V., Kokkinidis, M., and Glykos, N. M. (2009) Molecular dynamics simulations of *Bc*ZBP, a deacetylase from *Bacillus cereus*: Active site loops determine substrate accessibility and specificity. *J. Chem. Theory Comput. 5*, 3299–3311.
25. Kim, H. U., and Goepfert, J. M. (1974) A sporulation medium for *Bacillus anthracis*. *J. Appl. Bacteriol. 37*, 265–267.
26. Fisher, N., and Hanna, P. (2005) Characterization of *Bacillus anthracis* germinant receptors *in vitro*. *J. Bacteriol. 187*, 8055–8062.
27. Janes, B. K., and Stibitz, S. (2006) Routine markerless gene replacement in *Bacillus anthracis*. *Infect. Immun. 74*, 1949–1953.
28. Ouyang, S. P., Sun, S. Y., Liu, Q., Chen, J., and Chen, G. Q. (2007) Microbial transformation of benzene to *cis*-3,5-cyclohexadien-1,2-diols by recombinant bacteria harboring toluene dioxygenase gene *tod*. *Appl. Microbiol. Biotechnol. 74*, 43–49.
29. McLaughlin, R. E., and Ferretti, J. J. (1995) Electrotransformation of streptococci. *Methods Mol. Biol. 47*, 185–193.
30. Studier, F. W. (2005) Protein production by auto-induction in high density shaking cultures. *Protein Expression Purif. 41*, 207–234.
31. Newton, G. L., Ko, M., Ta, P., Av-Gay, Y., and Fahey, R. C. (2006) Purification and characterization of *Mycobacterium tuberculosis* 1-D-*myo*-inositol-2-acetamido-2-deoxy-α-D-glucopyranoside deacetylase, MshB, a mycothiol biosynthetic enzyme. *Protein Expression Purif. 47*, 542–550.
32. Calendar, R., and Berg, P. (1966) The catalytic properties of tyrosyl ribonucleic acid synthetases from *Escherichia coli* and *Bacillus subtilis*. *Biochemistry 5*, 1690–1695.
33. Segel, I. H. (1975) Enzyme Kinetics, John Wiley & Sons, New York.
34. Gosselin, S., Alhussaini, M., Streiff, M. B., Takabayashi, K., and Palcic, M. M. (1994) A continuous spectrophotometric assay for glycosyltransferases. *Anal. Biochem. 220*, 92–97.
35. Anderberg, S. J., Newton, G. L., and Fahey, R. C. (1998) Mycothiol biosynthesis and metabolism. *J. Biol. Chem. 273*, 30391–30397.
36. Otwinowski, Z., and Minor, W. (1997) Processing of X-ray diffraction data collected in oscillation mode. *Methods Enzymol. 276*, 307–326.
37. McCoy, A. J., Grosse-Kunstleve, R. W., Adams, P. D., Winn, M. D., Storoni, L. C., and Read, R. J. (2007) *Phaser* crystallographic software. *J. Appl. Crystallogr. 40*, 658–674.
38. Adams, P. D., Afonine, P. V., Bunkoczi, G., Chen, V. B., Davis, I. W., Echols, N., Headd, J. J., Hung, L. W., Kapral, G. J., Grosse-Kunstleve, R. W., McCoy, A. J., Moriarty, N. W., Oeffner, R., Read, R. J., Richardson, D. C., Richardson, J. S., Terwilliger, T. C., and Zwart, P. H. (2010) *PHENIX*: A comprehensive Python-based system for macromolecular structure solution. *Acta Crystallogr. D66*, 213–221.
39. Emsley, P., and Cowtan, K. (2004) Coot: Model-building tools for molecular graphics. *Acta Crystallogr. D60*, 2126–2132.
40. Holm, L., and Park, J. (2000) DaliLite workbench for protein structure comparison. *Bioinformatics 16*, 566–567.
41. DeLano, W. L. (2002) The PyMOL Molecular Graphics System, DeLano Scientific, San Carlos, CA.
42. Thompson, J. D., Higgins, D. G., and Gibson, T. J. (1994) CLUSTAL W: Improving the sensitivity of progressive multiple sequence alignment through sequence weighting, position-specific gap penalties and weight matrix choice. *Nucleic Acids Res. 22*, 4673–4680.
43. Gouet, P., Courcelle, E., Stuart, D. I., and Metoz, F. (1999) ESPript: Analysis of multiple sequence alignments in PostScript. *Bioinformatics 15*, 305–308.
44. Newton, G. L., Buchmeier, N., and Fahey, R. C. (2008) Biosynthesis and functions of mycothiol, the unique protective thiol of *Actinobacteria*. *Microbiol. Mol. Biol. Rev. 72*, 471–494.
45. Jothivasan, V. K., and Hamilton, C. J. (2008) Mycothiol: Synthesis, biosynthesis and biological functions of the major low molecular weight thiol in actinomycetes. *Nat. Prod. Rep. 25*, 1091–1117.
46. Sareen, D., Steffek, M., Newton, G. L., and Fahey, R. C. (2002) ATP-dependent L-cysteine:1-D-*myo*-inosityl 2-amino-2-deoxy-α-D-glucopyranoside ligase, mycothiol biosynthesis enzyme MshC, is related to class I cysteinyl-tRNA synthetases. *Biochemistry 41*, 6885–6890.
47. Newberry, K. J., Hou, Y. M., and Perona, J. J. (2002) Structural origins of amino acid selection without editing by cysteinyl-tRNA synthetase. *EMBO J. 21*, 2778–2787.
48. Passalacqua, K. D., Varadarajan, A., Ondov, B. D., Okou, D. T., Zwick, M. E., and Bergman, N. H. (2009) The structure and complexity of a bacterial transcriptome. *J. Bacteriol. 191*, 3203–3211.
49. Bergman, N. H., Passalacqua, K. D., Hanna, P. C., and Qin, Z. S. (2007) Operon prediction for sequenced bacterial genomes without experimental information. *Appl. Environ. Microbiol. 73*, 846–854.
50. Lobley, C. M., Schmitzberger, F., Kilkenny, M. L., Whitney, H., Ottenhof, H. H., Chakauya, E., Webb, M. E., Birch, L. M., Tuck, K. L., Abell, C., Smith, A. G., and Blundell, T. L. (2003) Structural insights into the evolution of the pantothenate-biosynthesis pathway. *Biochem. Soc. Trans. 31*, 563–571.
51. Saadat, D., and Harrison, D. H. (1999) The crystal structure of methylglyoxal synthase from *Escherichia coli*. *Structure 7*, 309–317.
52. Bergman, N. H., Anderson, E. C., Swenson, E. E., Janes, B. K., Fisher, N., Niemeyer, M. M., Miyoshi, A. D., and Hanna, P. C. (2007) Transcriptional profiling of *Bacillus anthracis* during infection of host macrophages. *Infect. Immun. 75*, 3434–3444.
53. Passalacqua, K. D., Bergman, N. H., Lee, J. Y., Sherman, D. H., and Hanna, P. C. (2007) The global transcriptional responses of *Bacillus anthracis* Sterne (34F2) and a Δ*sodA1* mutant to paraquat reveal metal ion homeostasis imbalances during endogenous superoxide stress. *J. Bacteriol. 189*, 3996–4013.
54. Fuchs, G. (1999) Biosynthesis of building blocks. In Biology of the Prokaryotes (Schlegel, H. G., Ed.) pp 110−160, Blackwell Science, Inc., Malden, MA.
55. Krepinsky, K., and Leimkühler, S. (2007) Site-directed mutagenesis of the active site loop of the rhodanese-like domain of the human molybdopterin synthase sulfurase MOCS3. Major differences in substrate specificity between eukaryotic and bacterial homologs. *FEBS J. 274*, 2778–2787.
56. Cao, M., Bernat, B. A., Wang, Z., Armstrong, R. N., and Helmann, J. D. (2001) FosB, a cysteine-dependent fosfomycin resistance protein under the control of σ^{W}, an extracytoplasmic-function σ factor in *Bacillus subtilis*. *J. Bacteriol. 183*, 2380–2383.
57. Guerin, M. E., Kordulakova, J., Schaeffer, F., Svetlikova, Z., Buschiazzo, A., Giganti, D., Gicquel, B., Mikusova, K., Jackson, M., and Alzari, P. M. (2007) Molecular recognition and interfacial catalysis by the essential phosphatidylinositol mannosyltransferase PimA from mycobacteria. *J. Biol. Chem. 282*, 20705–20714.
58. Rotzoll, N., Dunkel, A., and Hofmann, T. (2005) Activity-guided identification of (*S*)-malic acid 1-*O*-D-glucopyranoside (morelid) and γ-aminobutyric acid as contributors to umami taste and mouth-drying oral sensation of morel mushrooms (*Morchella deliciosa* Fr.). *J. Agric. Food Chem. 53*, 4149–4156.
59. Kleijn, R. J., Buescher, J. M., Le Chat, L., Jules, M., Aymerich, S., and Sauer, U. (2010) Metabolic fluxes during strong carbon catabolite repression by malate in *Bacillus subtilis*. *J. Biol. Chem. 285*, 1587–1596.
60. Errey, J. C., Lee, S. S., Gibson, R. P., Martinez-Fleites, C., Barry, C. S., Jung, P. M., O'Sullivan, A. C., Davis, B. G., and Davies, G. J. (2010) Mechanistic insight into enzymatic glycosyl transfer with retention of configuration through analysis of glycomimetic inhibitors. *Angew. Chem., Int. Ed. 49*, 1234–1237.
61. Mitchell, E. P., Withers, S. G., Ermert, P., Vasella, A. T., Garman, E. F., Oikonomakos, N. G., and Johnson, L. N. (1996) Ternary

complex crystal structures of glycogen phosphorylase with the transition state analogue nojirimycin tetrazole and phosphate in the T and R states. *Biochemistry 35*, 7341–7355.

62. Fersht, A. (1999) Structure and Mechanism in Protein Science, W. H. Freeman and Co., New York.
63. Mengin-Lecreulx, D., Allen, N. E., Hobbs, J. N., and van Heijenoort, J. (1990) Inhibition of peptidoglycan biosynthesis in *Bacillus megaterium* by daptomycin. *FEMS Microbiol. Lett. 57*, 245–248.
64. Day, W. A., Jr., Rasmussen, S. L., Carpenter, B. M., Peterson, S. N., and Friedlander, A. M. (2007) Microarray analysis of transposon insertion mutations in *Bacillus anthracis*: Global identification of genes required for sporulation and germination. *J. Bacteriol. 189*, 3296–3301.
65. Bergman, N. H., Anderson, E. C., Swenson, E. E., Niemeyer, M. M., Miyoshi, A. D., and Hanna, P. C. (2006) Transcriptional profiling of the *Bacillus anthracis* life cycle *in vitro* and an implied model for regulation of spore formation. *J. Bacteriol. 188*, 6092–6100.
66. Brown, D. W., Schaab, M. R., Birmingham, W. R., and Armstrong, R. N. (2009) Evolution of the antibiotic resistance protein, FosA, is linked to a catalytically promiscuous progenitor. *Biochemistry 48*, 1847–1849.
67. Buchmeier, N. A., Newton, G. L., Koledin, T., and Fahey, R. C. (2003) Association of mycothiol with protection of *Mycobacterium tuberculosis* from toxic oxidants and antibiotics. *Mol. Microbiol. 47*, 1723–1732.
68. Rukmana, A., Morimoto, T., Takahashi, H., Giyanto, and Ogasawara, N. (2009) Assessment of transcriptional responses of *Bacillus subtilis* cells to the antibiotic enduracidin, which interferes with cell wall synthesis, using a high-density tiling chip. *Genes Genet. Syst. 84*, 253–267.
69. Ortenberg, R. B., and Beckwith, J. (2003) Functions of thiol-disulfide oxidoreductases in *E. coli*: Redox myths, realities, and practicalities. *Antioxid. Redox Signaling 5*, 403–411.
70. Faulkner, M. J., Veeravalli, K., Gon, S., Georgiou, G., and Beckwith, J. (2008) Functional plasticity of a peroxidase allows evolution of diverse disulfide-reducing pathways. *Proc. Natl. Acad. Sci. U.S.A. 105*, 6735–6740.
71. Prinz, W. A., Åslund, F., Holmgren, A., and Beckwith, J. (1997) The role of the thioredoxin and glutaredoxin pathways in reducing protein disulfide bonds in the *Escherichia coli* cytoplasm. *J. Biol. Chem. 272*, 15661–15667.
72. Marty, L., Siala, W., Schwarzländer, M., Fricker, M. D., Wirtz, M., Sweetlove, L. J., Meyer, Y., Meyer, A. J., Reichheld, J.-P., and Hell, R. (2009) The NADPH-dependent thioredoxin system constitutes a functional backup for cytosolic glutathione reductase in *Arabidopsis*. *Proc. Natl. Acad. Sci. U.S.A. 106*, 9109–9114.
73. Kanzok, S. M., Fechner, A., Bauer, H., Ulschmid, J. K., Müller, H. M., Botella-Munoz, J., Schneuwly, S., Schirmer, R., and Becker, K. (2001) Substitution of the thioredoxin system for glutathione reductase in *Drosophila melanogaster*. *Science 291*, 643–646.
74. Gerdes, S. Y., Scholle, M. D., D'Souza, M., Bernal, A., Baev, M. V., Farrell, M., Kurnasov, O. V., Daugherty, M. D., Mseeh, F., Polanuyer, B. M., Campbell, J. W., Anantha, S., Shatalin, K. Y., Chowdhury, S. A., Fonstein, M. Y., and Osterman, A. L. (2002) From genetic footprinting to antimicrobial drug targets: Examples in cofactor biosynthetic pathways. *J. Bacteriol. 184*, 4555–4572.